Twin Wind tunnels for Energy & the EnvironmenT
INNOVATIONS - EXCELLENCE

Twin Tests Book of Reference

Twin Test 3/4
Microdevices for enhanced performance of airfoil sections

Lead Beneficiary: KIT
Dissemination Level: Public

Authors: K. Kellaris, L. Calzoni,
M. Manolesos, A. Croce

Deliverable 4.1

WP4

Widening of technical capacity and competence

TWEET-IE / Twin Wind tunnels for Energy and the
EnvironmenT - Innovations and Excellence
HORIZON-WIDERA-2021-ACCESS-03-01 / PR# 101079125

Co-funded by
the European Union

History and Changes

Ver	Date	Description	Contributors
1.0	28/08/2025	Initial Draft	NTUA, POLIMI
1.1	30/09/2025	Final	NTUA, POLIMI

Co-funded by
the European Union

Executive Summary

This chapter presented the facilities, equipment and set up details for the two campaigns carried out in the wind tunnels of the National Technical University of Athens (NTUA) and Politecnico di Milano (POLIMI) within the scope of Twin Test 3 of the TWEET-IE project. Namely, Twin Tests were conducted assessing the effect of micro devices for enhanced performance of flatback airfoil sections. The utter goal was to investigate the effect of freestream turbulence intensity, Reynolds number and blockage ratio on airfoil performance, 3D flow separation and wake behaviour. Additionally, the effect of flow control devices regarding flow separation control and drag reduction were assessed. The results between the two facilities deviate significantly even at the baseline case, which at this stage is attributed to 3D separated flow and differences in blockage. When fixing the boundary layer transition case over the airfoil surface, force and pressure timeseries demonstrate a switching behaviour between intermittent states in both facilities but at different rangers of AoAs and at different timescales. The use of Vortex Generators (GF) for flow separation control has a positive effect in both facilities. Additionally, using a Gurney flap leads to an increase in lift force (almost doubling it), but it comes with an increase in drag at both facilities, leading to small aerodynamic performance gains, especially at low AoAs. Finally, the effectiveness of placing drag reduction devices at or near the Trailing Edge (TE) of the airfoil (VGs and tabs) varies between facilities. Namely, at NTUA the aerodynamic performance is increased in a similar way for the TE VGs and TE tabs, (25%), while the improvement is marginal (approximately 1%) for the POLIMI tests.

Co-funded by the European Union

Table of Contents

List of Figures

List of Tables

1 Introduction

The need for lower Levelized Cost of Energy (LCOE) for wind energy, requires, among others, an increase in rotor diameter for modern Wind Turbines. Consequently, the need for novel solutions that can support this size increase arises. One of these solutions is the use of flatback (FB) airfoils, i.e. airfoil profiles with a blunt trailing edge (TE), at the root region of the Wind Turbine blade as they provide several aerodynamic, structural, and aeroelastic advantages [1]. Namely, FB airfoils can provide higher lift values due to the reduced adverse pressure gradient over the aft part of the suction side [1]. In addition, their aerodynamic performance is insensitive to surface roughness when compared to that of traditional sharp TE airfoils when certain design conditions are met [1]. Early studies performed on the $100m$ long SNL100-03 blade designed by Sandia National Laboratories, showed that, blades with FB airfoils can be up to 16% lighter than blades with traditional airfoils [2]. Additionally, due to the blunt TE and increased blade cross-sectional area, FB blades have increased flapwise stiffness.

These benefits, however, come with an increase in profile drag. Furthermore, due to their relatively high thickness, they may exhibit three-dimensional flow separation both at their pressure and suction side. The maximum lift is observed at relatively low angles of attack and for certain cases the lift curve may exhibit a minimum in between two maximums. Flow separation also leads to a bifurcating behaviour, related to three-dimensional instabilities, that can be observed in the load and pressure timeseries. This observation, in conjunction with the vortex shedding from the blunt TE, makes experimental studies of FB airfoils a troublesome endeavour. Additionally, the scarcity of relevant experimental studies [1, 3, 4, 5, 6], makes clear the need to investigate the effects of different WT facilities and operating conditions on FB airfoil performance and behaviour.

Here, we present a Twin Wind Tunnel Test for a FB airfoil at two different facilities that took place in Spring 2025. The utter goal is to investigate the effect of freestream turbulence intensity, Reynolds number and blockage ratio on airfoil performance, 3D flow separation and wake behaviour. Wind tunnel tests were carried out in two of the partners of the TWEET-IE project, namely at the National Technical University of Athens (NTUA) and at Politecnico di Milano (POLIMI).

1.1 Twin Wind Tunnel Test outline

In both facilities, the same model was be tested. Namely, the FB4286-0802 airfoil, shown in fig. 1, present in the SNL-03 reference wind turbine [2]. The maximum thickness of the model is 42.86% of the chord and the TE thickness is 8.02% of the chord. The chord length is $c = 0.5m$ and the model span is $1m$, leading to an aspect ratio of $AR = 2$. Different setups were be used in each facility with the same model. A summary of the employed measurement technqiques at each facility is shown in table 1.

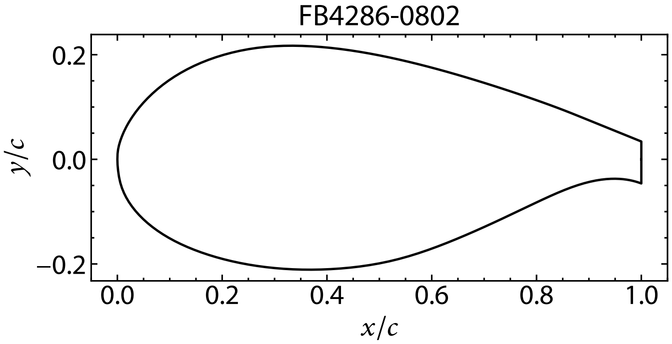

Figure 1: The FB4286-0802 profile.

Table 1: Summary of the Twin Test.

Facility	Surface Pressure	Hot-wire	Balance	Tufts	SPIV	Reynolds number	Transition
NTUA	✓	✓	✗	✓	✓	1.25×10^6	Both
POLIMI	✓	✓	✓	✗	✗	1.18×10^6	Both

2 Setups & measuring methods

2.1 General description of the NTUA setup

The NTUA wind tunnel [7] tests took place in the small test section of the closed-loop Wind Tunnel belonging to the Scool of Mechanical Engineering. The test section is an octagon with main dimensions $1.4\text{m} \times 1.8\text{m}$ (height × width). The maximum achievable wind speed in the test section is 45m/s and the turublence intensity (TI) is lower than 0.2%. The model is placed vertically inside the test section, with endplates mounted on both sides in order to minmize tip effects and the influence of the boundary layer (BL) of the WT walls. Additionally, the model is extended vertically up to 0.5cm from the WT walls with wooden extensions ensuring an even pressure distribution. The resulting bloackage ratio is 11.9%. The setup is shown in fig. 2. Outside of the test section, the models' top shaft is coupled to a stepper motor that controls the angle of attack (AoA). Additionally, an angular displacement sensor is coupled to the bottom shaft of the model, measuring the AoA. The freestream dynamic pressure was measured using a Pitot tube as well as the static perrssure drop along the contraction nozzle before the test section. Additonally, freestream absolute pressure and temperature were also measured. The NTUA tests included surface pressure measurements, hot-wire measurements and Stereo PIV measurements. Both fixed and free transition cases were tested at a Reynolds number of Re $= 1.25 \times 10^6$. The transition of the boundary layer (BL) state from laminar to turbulent was fixed by placing zig-zag tape with a height of $h_{zig-zag} = 0.125$ mm at both sides of the airfoil at chordwise locations of $5\%c$ and $10\%c$ at the suction and pressure sides, respectively.

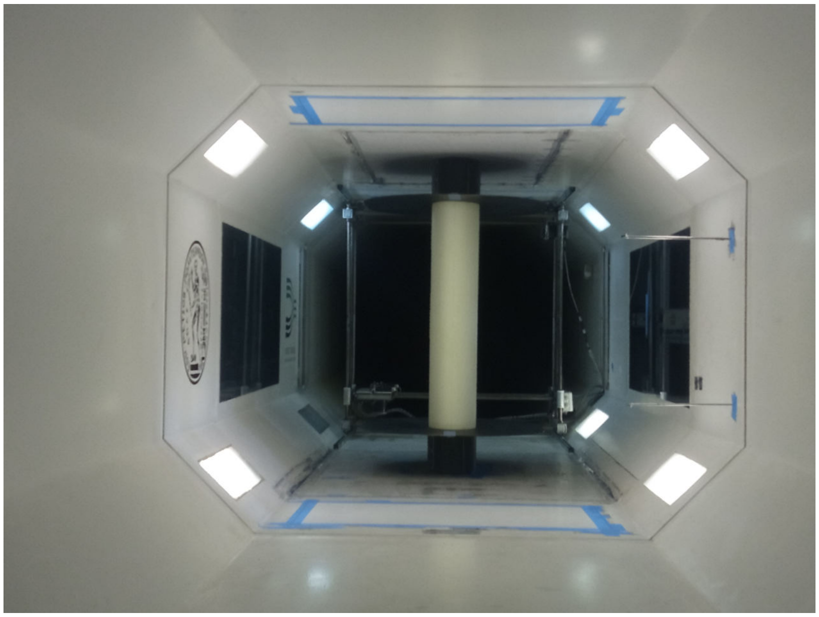

Figure 2: Downstream view of the model inside the NTUA test section.

2.1.1 Surface pressure measurements

31 pressure taps were connected to a 32-channel μDAQ2 DTC pressure scanner from Chell Instruments. The reference pressure was the static pressure in the inlet of the test section. The sampling frequency was $f_{s,\text{pressure}} = 1\text{kHz}$ and the acquisition time was typically equal to $\Delta t_{\text{acquisition,pressure}} = 60\text{s}$.

2.1.2 Hot-wire measurements

Single component measurements were taken using hot-film sensors made by TSI. The IFA-300 system of TSI was used with a calibrator also manufactured by TSI. The probe was positioned $\approx 0.85c$ downstream of the airfoil TE. Measurements were taken at a sampling rate of $f_{s,\text{HW}} = 20\text{kHz}$ with a low pass filter of $f_{lp} = 10\text{kHz}$. The total acquisition time was $\Delta t_{\text{acquisition,HW}} \approx 50\text{s}$ The setup is shown in fig. 3.

Figure 3: NTUA hot-wire setup.

2.1.3 Stereo PIV setup

All measurements concern a plane normal to the wing axis at the center of its span. The cameras were located above and below the test section, i.e. at a vertical distance of 70cm the center plane. The horizontal distance from the wing TE is 110cm or $2.2c$, and the camera-contained angle (ϕ) was $\phi \approx 2\tan^{-1}\left(\frac{70\text{cm}}{110\text{cm}}\right) = 65^\circ$; see fig. 4.

All stereo PIV measurements were taken with the wing at neaer-zero AoA and at $\text{Re} = 1.25 \times 10^6$. For each case, 1000 snapshots were taken and it is important to note that each snapshot was measured in syncronously with pressure with a time interval between snaphots $\Delta t_{\text{snapshot}} \approx 2.25\text{s}$. The pulse separation time for each snapshot was $\Delta\tau = 18\,\mu\text{s}$. A 200 mJ Nd:YAG PIV laser (Litron Lasers) with dual cavities was used to create a 1.8-mm-thick light sheet at the measurement plane using the 90% power of the laser. The flow was seeded with oil droplets of 1 μm mean diameter created by a commercial generator (TSI model 9307). Two 12 bit TSI Powerview Plus 4 megapixel Cameras with Sigma 150 mm f/2.8 lenses were used to obtain the data. After stereoscopic reconstruction, the resulting measured plane has dimensions of 19.5cm × 11.6 cm (width × height).

Regarding processing, firstly a background image was removed from each captured snapshot, Then, an iterative image deformation algorithm was utilized starting from an interrogation window of 64 × 64 and ending to an interrogation window of 32 × 32.

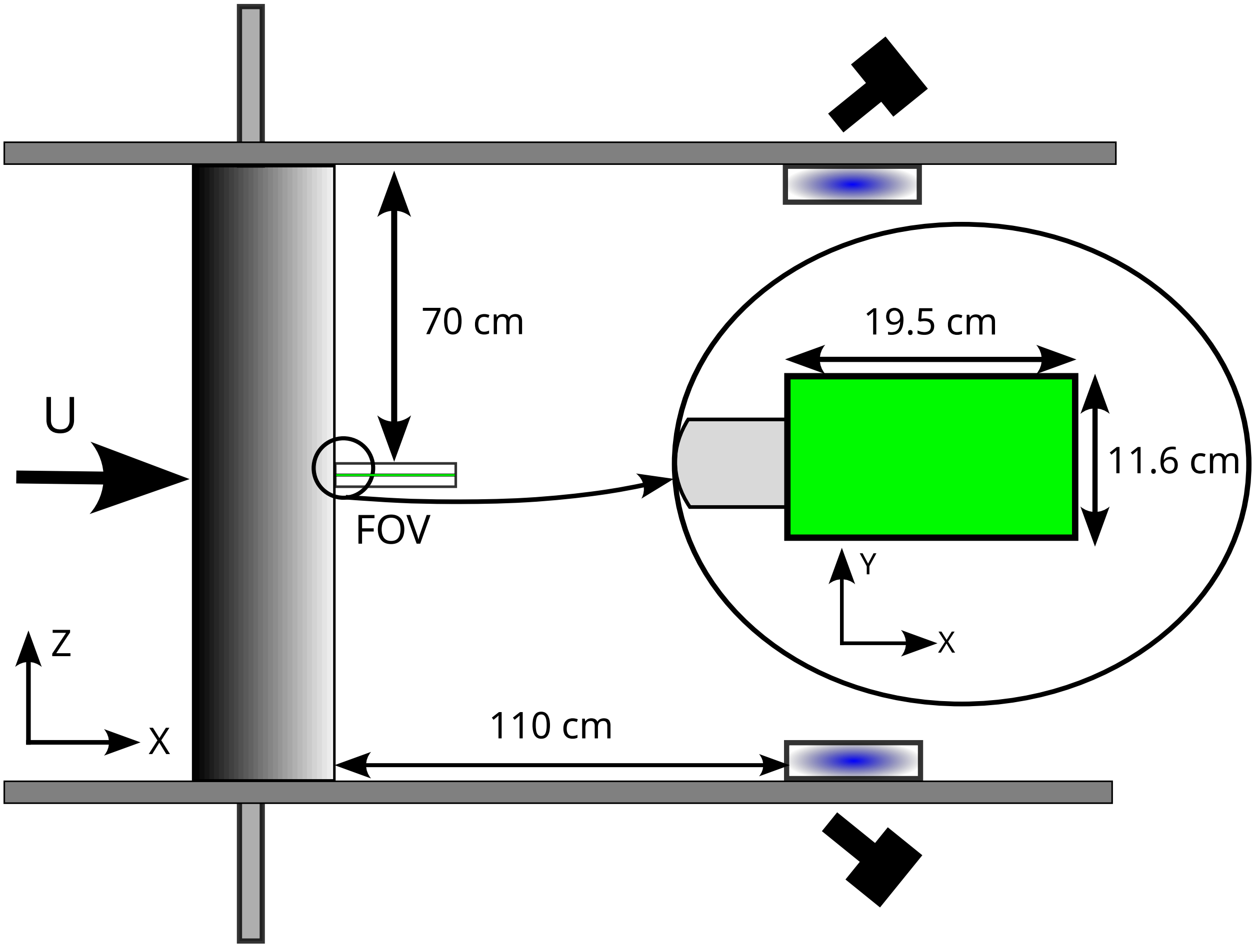

Figure 4: Sketch of the Stereo PIV Setup at NTUA.

2.2 General description of the POLIMI setup

The POLIMI wind tunnel experiments were conducted in the Low Turbulence Test Section of the Galleria del Vento del Politecnico di Milano (GVPM). This facility is a closed-circuit wind tunnel with a vertical layout, featuring two test sections located on opposite sides of the loop. The lower section (the Low Turbulence Test Section), used in this Twin Test, is designed for low-turbulence experiments. The upper section, larger in size, is intended for civil engineering testing (the Boundary Layer Test Section). The Low Turbulence Test Section offers two interchangeable test chambers, allowing setup preparation and assembly outside the main loop. This minimizes wind tunnel downtime and enables experiments to be prepared while other tests are conducted in either test section.

The facility is powered by an array of 14 fans, each 1.8 m in diameter and 100 kW, giving a total installed power of 1.4 MW. The fans are arranged in two rows of seven $2 \times 2\,\text{m}$ independent cells. The test section used for these experiments measures $4m$ in length, with a cross-section of $4\,\text{m} \times 3.84\,\text{m}$. The maximum wind velocity is 55 m/s, with a free-stream turbulence intensity below 0.1%, while the model blockage is approximately 1.88%. Further technical details regarding the wind tunnel are provided in [8].

The POLIMI tests included surface pressure measurements, force balance measurements, and hot-wire measurements. Surface pressure measurements were used to determine the basic aerodynamic performance of the airfoil and to compare results between facilities. Force balance measurements provided insight into the effect of three-dimensional separation on airfoil loads, while hot-wire measurements were used to assess spanwise wake correlations. Both fixed and free transition cases were tested at a Reynolds number of $\text{Re} = 1.18 \times 10^6$. The transition of the boundary layer (BL) state from laminar to turbulent was fixed by placing zig-zag tape with a height of $h_{zig-zag} = 0.125\,\text{mm}$ at both sides of the airfoil at chordwise locations of $5\%c$ and $10\%c$ at the suction and pressure sides, respectively.

2.2.1 Model preparation

The model, the same as that used in the NTUA experiments, was mounted vertically in the Low Turbulence Test Section with a custom setup designed specifically for this study; see fig. 5. Ideally, for airfoil performance characterizations, the airfoil would span the full height of the test section, as in the NTUA test section, allowing for a wall-to-wall model. This is important for achieving truly two-dimensional airfoil performance measurements, as it minimizes the influence of tip effects and sidewall interference, which can introduce three-dimensional flow features that alter the aerodynamic loads and pressure distribution.

The model was mounted vertically rather than horizontally. Mounting it horizontally would have required extensions to the model to create a wall-to-wall configuration, effectively changing the aspect ratio of the airfoil. Additionally, the hot-wire correlation measurements required the model to be as low as possible in the test section, since the traversing system, described in detail in section 2.2.4, is designed to measure spanwise velocities in the inner, central portion of the model. Due to these main constraints, the vertical mounting with endplates was chosen as the optimal setup.

The endplates were carefully designed to preserve as much two-dimensionality as possible. They help reduce spanwise flow near the tips, mitigating the development of vortices, as well as minimize the influence of the BL formed in the WT walls. The placement, gap size, and support of the end plates were carefully chosen to balance structural stability and aerodynamic fidelity. In detail, the lower endplate is not attached directly to the airfoil but is positioned on a table constructed from Bosch elements, leaving a $5\,\text{mm}$ gap between the model and the end plate. The upper end plate was installed similarly; however, to ensure proper decoupling from the model, an external support, show in fig. 5(a), was used. The gaps between the endplates and the model where $0.5\,\text{cm}$ or $\approx 0.5\%$ of the model span, well within the suggested gaps by the literature [9].

(a)

(b)

Figure 5: (a) View fo the installed model at the GVPM. (b) CAD Assembly of the setup.

2.2.2 Surface pressure measurements

63 pressure taps are located at the centre-line of the model. Their locations can be seen in fig. 6(a). A pressure measurement system consisting of tubes mounted on the pressure taps and connected via two quick connectors to two 32-channel ESP-32HD-DTC pressure scanners, allowing for the acquisition of synchronous measurements for all pressure taps, compared to NTUA where only 32 taps were used. The tubing system inside the model is shown in fig. 6(b). The total and static pressures were also measured at the same time. A Pitot tube was used in both cases. The sampling frequency was $f_{s,\text{pressure}} = 500\,\text{Hz}$ and the acquisition time was typically equal to $\Delta t_{\text{acquisition,pressure}} = 30\,\text{s}$. For specific cases where flow separation behaviour is more complex, larger acquisition times were used.

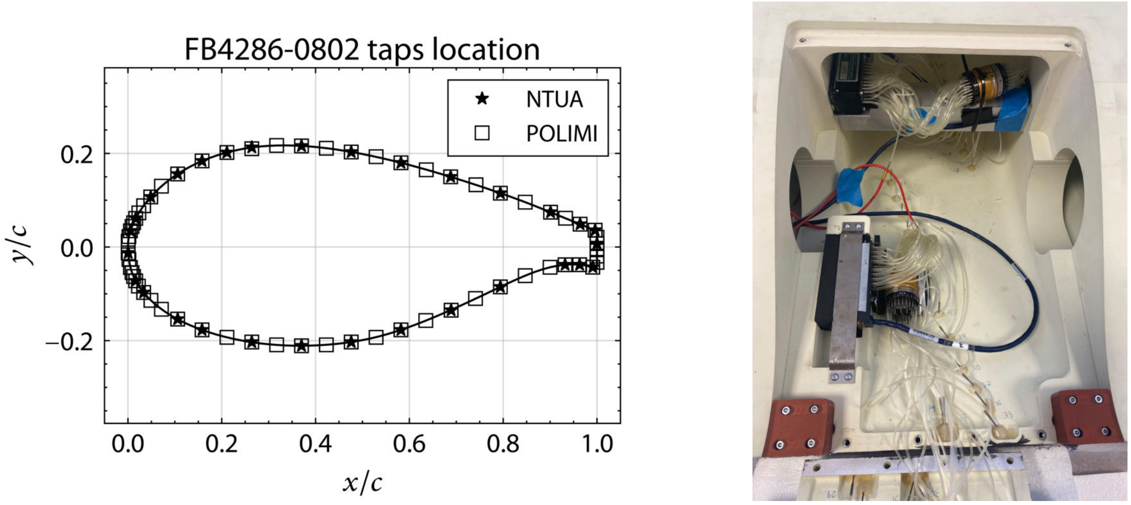

(a)

(b)

Figure 6: (a) Pressure taps positioning. (b) View of the tubing inside the model.

2.2.3 Balance measurements

In the setup at POLIMI, the use of a balance was integrated already during the design phase. The balance employed is a RUAG 192-6L Balance and measurements were taken for $\Delta t_{\text{acquisition,balance}} = 30\,\text{s}$ with a sampling rate of $f_s = 1\,\text{kHz}$ As shown in fig. 7(a), it was mounted on a specially prepared plate installed on the turntable, allowing it to rotate together with the model. Therefore, the measured forces were the normal and tangent components, here aligning with the F_x and F_y components of the balance and a rotation was required to obtain lift and drag; see section 2.3.1. A second custom-designed plate was used to connect the balance with the model through a clamp-like system that prevented any undesired movement of the model; see fig. 7(a). To protect the balance from direct exposure to the oncoming airflow, a circular polystyrene structure (fairing) was installed around it, thereby isolating the instrument and avoiding possible measurement disturbances. Particular care was taken to ensure that the endplates, were not included in the forces measured by the balance as the whole fairing structure was not in direct contact with either the model or the balance, as shown in fig. 7(b).

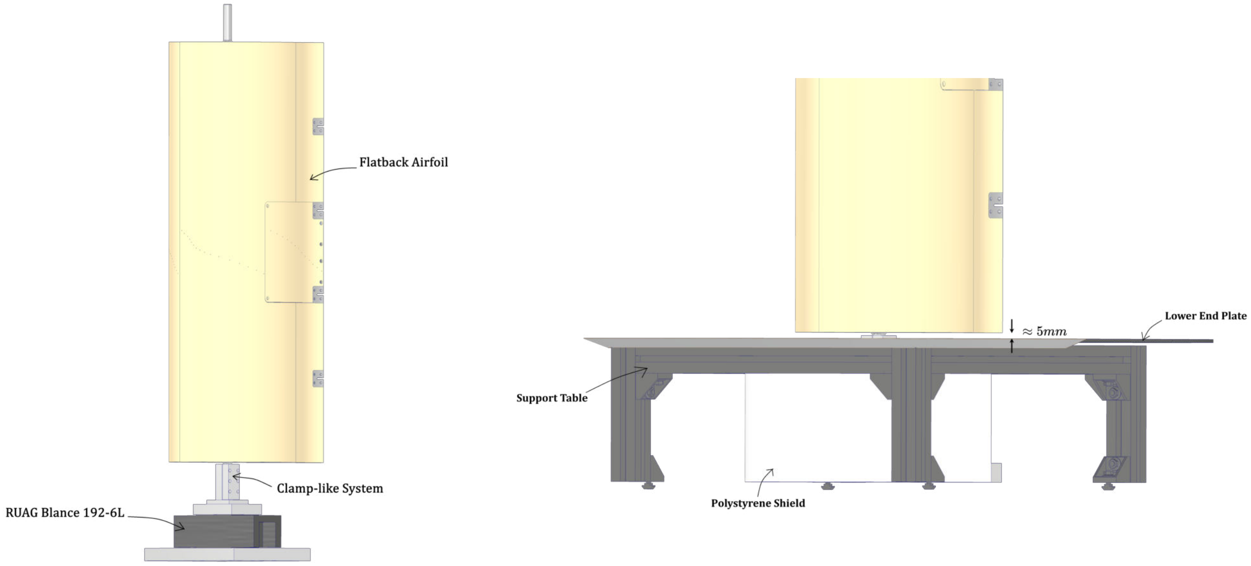

(a) (b)

Figure 7: (a) Side view of the constructed mounting mechanism. (b) Assembly of the balance fairing.

2.2.4 Hot-wire measurements

In order to characterize the wake generated by the FB airfoil, hot-wire measurements were also carried out. A dedicated setup was developed, shown in fig. 8, incorporating two triple-hotwire probes, namely two tri-axial fiber-film probes from Dantec Dynamics, that are capable of simultaneously measuring the three velocity components and capturing turbulent fluctuations with high temporal resolution. The probes were arranged in a correlated configuration. One probe, serving as a fixed reference, was positioned at a defined height and remained stationary throughout the measurements. The second probe was mounted on a dedicated support system that allowed controlled movement relative to the fixed one, while ensuring vertical alignment to preserve spatial correlation between the two signals.

The support structure consisted of a main column equipped with vertical rails along which a sliding plate could be fixed at the desired height. Two cylindrical supports were installed on the plate: one for the fixed probe and one for the movable probe, as shown in fig. 8(a). The reference probe was positioned at 20% of the chord length above the lower edge of the airfoil, ensuring stable placement within the wake. The movable probe, mounted on a motorized translation system, was displaced in the spanwise direction while maintaining strict alignment with the reference probe.

The initial spacing between the probes was carefully selected to avoid aerodynamic interference while complying with the mechanical constraints of the support system. Namely, the initial distance was equal to $\Delta_{z,\text{initial}} \approx 1h_{TE}$, while the step of the vertical movement was $\delta_z = 4\,\text{mm} \approx 0.1h_{TE}$. Both probes were placed downstream of the trailing edge at approximately 60% of the chord length, as shown in fig. 8(b). This configuration enabled systematic scanning of the central span region, away from tip vortices, providing a clear characterization of the typical wake features of the flatback geometry. The acquisition was carried out at a sampling rate of $f_s = 2.5\,\text{kHz}$ for a total time $\Delta_{\text{acqusition,HW}} = 30\,\text{s}$ per point. Finally, the calibration was carried out in-situ with the model removed.

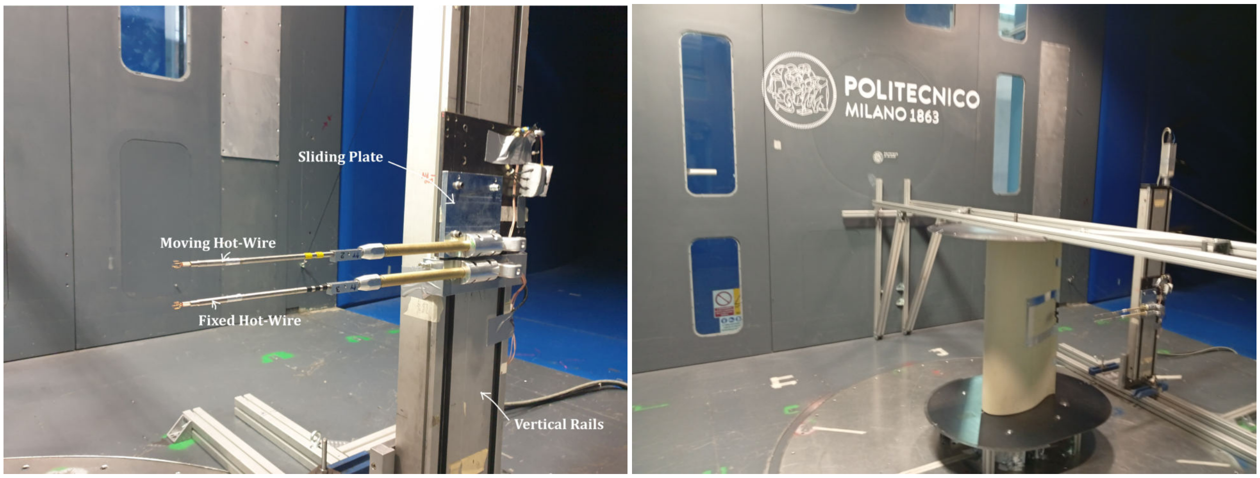

(a)

(b)

Figure 8: (a) The installed traversing system. (b) The traversing system in relation to the installed model.

2.3 Data reduction

2.3.1 Integration of surface pressure distribution

The pressure coefficient for the i-th pressure tap is defined as:

$$C_{p,i} = \frac{p_{\text{static},i} - p_{\text{static},\infty}}{q_\infty} \tag{1}$$

where $q_\infty = \frac{1}{2}\rho U_\infty^2$ is the dynamic pressure of the freestream, with ρ and U_∞ being the freestream density and velocity respectively, Next, the lift C_L and pressure drag $C_{D,p}$ coefficients, defined as:

$$C_L = \frac{L}{q_\infty c} \tag{2}$$

$$C_{D,p} = \frac{D}{q_\infty c} \tag{3}$$

can be easily calculated by integrating the pressure coefficient (C_p) distribution around the airfoil (see for example [9] or [10]).

Firstly, we calculate the forces at the normal and tangent directions of the airfoil surface by projecting the pressure that is, by definition, normal to the airfoil elemental surface on the respective dimensions and then integrating it, as shown in Figure 9. Therefore, the normal and tangent force coefficients (for unitary span) are given by:

$$C_N = \frac{1}{c}\oint C_p \cos\theta \mathrm{d}s = \frac{1}{c}\int C_p \mathrm{d}x \tag{4}$$

$$C_T = \frac{1}{c}\oint C_p \left(-\sin\theta\right) \mathrm{d}s = \frac{-1}{c}\int C_p \mathrm{d}y \tag{5}$$

If the pressure taps are ordered counterclockwise around the airfoil, the above expressions can be easily turned into simple summations using the trapezoid rule:

$$C_N \approx \frac{1}{c}\sum_{i}^{N_{\text{taps}}-1} \frac{1}{2}\left(C_{p,i} + C_{p,i+1}\right)\left(x_{i+1} - x_i\right) \tag{6}$$

$$C_T \approx \frac{-1}{c}\sum_{i}^{N_{\text{taps}}-1} \frac{1}{2}\left(C_{p,i} + C_{p,i+1}\right)\left(y_{i+1} - y_i\right) \tag{7}$$

We can calculate the moment coefficient around the leading edge $C_{m_{LE}}$ in a similar way as:

$$C_{m_{LE}} = \frac{-1}{c^2}\int C_p x \mathrm{d}x - \frac{1}{c^2}\int C_p y \mathrm{d}y \tag{8}$$

$$C_{m_{LE}} = \frac{-1}{c^2}\sum_{i}^{N_{\text{taps}}-1} \frac{1}{2}\left\{\left(C_{p,i}x_i + C_{p,i+1}x_{i+1}\right)\left(x_{i+1} - x_i\right) + \left(C_{p,i}y_i + C_{p,i+1}y_{i+1}\right)\left(y_{i+1} - y_i\right)\right\} \tag{9}$$

Next, we need to project the normal and tangent components back to the *global* system in order to obtain the lift and drag coefficients for unitary span, giving:

$$C_L = C_N \cos\alpha - C_T \sin\alpha \tag{10}$$

$$C_{D,p} = C_N \sin\alpha + C_T \cos\alpha \tag{11}$$

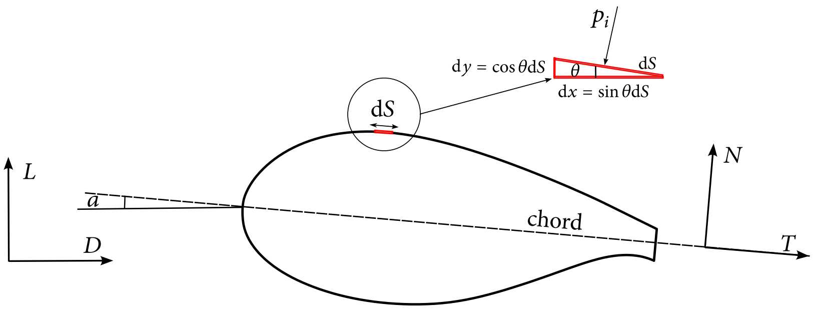

Figure 9: Pressure integration around an airfoil profile.

The same transformation is carried out for the balance data, as the balance is aligned with the *local* airfoil coordinate system and rotates with it, as shown below

$$
\begin{aligned}
C_{l,\text{balance}} &= C_{N,\text{balance}} \cos\alpha - C_{T,\text{balance}} \sin\alpha & (12)\\
C_{d,\text{balance}} &= C_{N,\text{balance}} \sin\alpha + C_{T,\text{balance}} \cos\alpha & (13)
\end{aligned}
$$

where

$$
\begin{aligned}
C_{N,\text{balance}} &= \frac{F_x}{q_\infty c} & (14)\\
C_{T,\text{balance}} &= \frac{F_y}{q_\infty c} & (15)
\end{aligned}
$$

2.3.2 Dynamic pressure response

The standard approach to model the dynamic pressure response of the tubing system is the one developed by [11]. In this method the unsteady longitudinally varying fluid partial differential equations are integrated in the frequency domain to give an end-to-end frequency response model. This solution can only be written in the frequency domain. The resulting end-to-end input/output transfer function is

$$
\frac{P_L(\omega)}{P_0(\omega)} = \Upsilon(\omega) = \frac{1}{\cosh\left[\omega\Gamma_p \frac{L}{c}\right] + \frac{V\omega\Gamma_p}{A_c c} \sinh\left[\omega\Gamma_p \frac{L}{c}\right]} \tag{16}
$$

where $P_0(\omega)$ and $P_L(\omega)$ are the frequency domain representations of $p_0(t)$ and $p_L(t)$. Additionally, the parameter c is the local sonic velocity, A_c is the tube cross-sectional area, and Γ_p is the wave propagation factor. The cross-sectional area is assumed to be constant. As derived by [11] for continuum flow conditions the most general form of the propagation factor is

$$
\Gamma_p = \sqrt{\frac{\gamma J_0(\alpha)}{\xi} - 1} \tag{17}
$$

where α is the shear wave number given by

$$
\alpha = \left(\frac{j^{3/2}}{2}\right)\sqrt{\frac{\omega \rho_0 D^2}{\mu}} \tag{18}
$$

In eq. (18) the parameter μ is the dynamic viscosity of the working fluid, ρ_0 is the longitudinal mean fluid density in the tube, and J_0, J_2 are zero and second-order Bessel functions of the first kind. The parameter, ξ, models the wave expansion compression as a polytropic process. Generally, ξ is complex valued and is dependent on the input wave frequency. The variation of ξ with the shear wave number is given by

$$
\xi = \frac{1}{1 + \frac{\gamma - 1}{\gamma} \frac{J_2(\sqrt{P_r}\alpha)}{J_0(\sqrt{P_r}\alpha)}} \tag{19}
$$

The deconvolution of $P_L(\omega)$ with $\Upsilon(\omega)$ provides an estimation of the surface pressure $\hat{P}_0(\omega)$. However, this can result in increased amplification of $P_L(\omega)$ with increasing frequency and when $\hat{P}_0(\omega)$ is transformed to the time domain, this amplification at high frequencies results in a noise dominated signal [12]. Therefore, a deconvolution that reconstructs the surface pressure signal without amplifying the measurement noise is desired. In order to achieve this, [12] suggested the use of the Wiener deconvolution [13]. Namely, an optimal filter $G(\omega)$ is used in place of $\Upsilon^{-1}(\omega)$ such that:

$$\hat{P}_0(\omega) = G(\omega) P_L(\omega) \tag{20}$$

The filter function $G(\omega)$, proposed by [12] aims to minimize the difference between actual and estimated surface pressures when noise is present on $p_L(t)$, and is given by

$$G(\omega) = \frac{\Upsilon^* \left(\frac{||P_0||^2}{||N||^2}\right)}{||\Upsilon||^2 \left(\frac{||P_0||^2}{||N||^2}\right) + 1} \tag{21}$$

where the quantity $\left(\frac{||P_0||^2}{||N||^2}\right)$ can be considered as an approximation of the squared signal to noise ratio, SNR, which in typically approximated as

$$\text{SNR} \approx \frac{\left\|\mu_{P_L}\right\|}{\sigma_{P_L}} \tag{22}$$

where μ_{p_L} is the mean and σ_{p_L} is the standard deviation of $p_L(t)$. However, this approach is insufficient for cases where the underlying physics influence the ratio μ/σ. A better approach, inspired from [14], is to estimate SNR as:

$$\text{SNR} \approx 10 \log_{10} \frac{P_{p_L}}{P_{\text{noise}}} \tag{23}$$

where P_{p_L} and P_{noise} are the power of $p_L(t)$ and the estimated noise, respectively. The noise is estimated by taking pressure measurements with the same parameters without the WT operating. The power P_x of a time signal $x(t)$ with a duration of T is given by:

$$P_x = \frac{1}{T} \sum_{t=0}^{T} \left\|x^2(t)\right\| \tag{24}$$

2.4 Wind tunnel corrections

The conditions in a wind tunnel do not allow the flow to develop precisely the same way, as in free air. For airfoil sections spanning the tunnel, the variation in static pressure along the axis of the test section is considered insignificant. However, the walls create the following constraints:

- The area through which the flow passes around a model is reduced, due to the presence of the wind tunnel walls (solid blockage), which essentially increases the free stream velocity near the model.
- On the contrary, the wake generated by the model in the test section respectively “blocks” an area downstream of the model, which increases the velocity outside the wake and in turn creates a pressure gradient. This is referred to as wake blockage.
- Finally, the walls cause a confinement known as streamline curvature, which limits the development of the curvature of the free stream.

2.4.1 NTUA

Here, corrections regarding the aforementioned effects are accounted for following the works of [15] and [16]. Specifically, for a model of chord c and tunnel breadth h, the parameter σ is defined as:

$$\sigma = \frac{\pi^2 c^2}{48\beta^2 h^2} \tag{25}$$

where $\beta = \sqrt{1 - M_0^2}$ is the compressibility factor, with M_0 being the upstream Mach number. The coefficients for solid ϵ_{sb} and wake ϵ_{wb} blockage are given by:

$$\epsilon_{sb} = \frac{\pi}{6}\frac{\mathrm{A}}{\beta^3 h^2} \tag{26}$$

$$\epsilon_{wb} = \frac{1}{4}\frac{c}{\beta^2 h} C_D \tag{27}$$

$$\epsilon = \epsilon_{sb} + \epsilon_{wb} \tag{28}$$

where A is the effective airfoil cross-sectional area. Typically, the variation of A with AoA is given by:

$$\frac{\mathrm{A}}{c^2} = \left(1 + 1.2\beta\frac{t}{c}\right)\left(1 + 1.1\frac{c}{t}\beta\alpha^2\right)\frac{\mathrm{A}_{geom}}{c^2} \tag{29}$$

where t is the max thickness of the airfoil and A_{geom} is the cross-sectional area of the airfoil. At higher AoA, either positive or negative, the stall of the airfoil gives rise to a region of separated flow that occupies a significant volume of the test section. This effect strongly increases the effective cross-section [17] and can be accounted for [18]:

$$\frac{\mathrm{A}_M}{c^2} = \frac{3}{\pi}\frac{\beta^3}{2 - M^2}\frac{h^2}{c^2}\left(-1 + \sqrt{1 + 4\frac{c}{h}C_{D_M}}\right) \tag{30}$$

This additional effective cross-section A_M due to the volume occupied by flow separation, computed from Maskell's method [19], should be added to the effective cross-section of the airfoil without flow separation. The increase in drag coefficient associated to flow separation C_{D_M} is taken as the uncorrected drag coefficient, minus the minimum drag coefficient of the polar curve: $C_{D_M} = C_D - C_{D,min}$, as measured from the surface pressures. The AoA is corrected for lift interference as:

$$\alpha' = \alpha + \frac{57.3\sigma}{2\pi}\left(C_L + 4C_m\right) \tag{31}$$

Finally, the corrected coefficients become:

$$C_L' = C_L\left(1 - \sigma - 2\epsilon\right) \tag{32}$$

$$C_D' = C_D\left(1 - 3\epsilon_{sb} - 2\epsilon_{wb}\right) \tag{33}$$

$$C_m' = C_m\left(1 - 2\epsilon\right) + \frac{1}{4}\sigma C_L' \tag{34}$$

where the $'$ symbols represent the corrected coefficients. It is important to note that C_m is the moment coefficient at the quarter chord point, i.e. $C_m = C_{m_{c/4}}$. Therefore, before the correction, we convert the $C_{m_{LE}}$ to $C_{m_{c/4}}$ as:

$$C_{m_{c/4}} = C_{m_{LE}} + \frac{c}{4}C_L \tag{35}$$

then apply the corrections to $C_{m_{c/4}}$ and convert back to $C_{m_{LE}}$.

Co-funded by the European Union

2.4.2 POLIMI

Standard three-dimensional wind-tunnel corrections are applied [9]. The solid blockage correction factor ϵ_{sb} is given by:

$$\epsilon_{sb} = \frac{KV_{\text{model}}}{\beta^3\sqrt{C^3}} \tag{36}$$

where $K = 0.9$, V_{model} is the model volume and C is the wind tunnel cross-sectional surface, for the POLIMI WT, C=$3.84\text{m} \times 4\text{m} = 15.36\text{m}^2$. The solid blockage is also calculated for the fairing construction, leading to:

$$\epsilon_{sb,\text{total}} = \epsilon_{sb,\text{model}} + \epsilon_{sb,\text{fairing}} \tag{37}$$

The wake blockage correction factor is the given by:

$$\epsilon_{wb} = \frac{S}{4\beta^2 C} C_D \tag{38}$$

with S being the model surface. Thus, the dynamic pressure can be corrected as:

$$q_{corr} = q(1 + 2\epsilon_{sb} + 2\epsilon_{wb}) \tag{39}$$

And consequently the force coefficients can be recalculated as:

$$C'_L = \frac{L}{q_{corr}S} = \frac{L}{qS}\frac{q}{q_{corr}} = C_L\frac{1}{1 + 2\epsilon_{sb} + 2\epsilon_{wb}} \tag{40}$$

$$C'_D = \frac{D}{q_{corr}S} = \frac{D}{qS}\frac{q}{q_{corr}} = C_D\frac{1}{1 + 2\epsilon_{sb} + 2\epsilon_{wb}} \tag{41}$$

$$C'_m = \frac{M}{q_{corr}Sc} = \frac{M}{qSc}\frac{q}{q_{corr}} = C_m\frac{1}{1 + 2\epsilon_{sb} + 2\epsilon_{wb}} \tag{42}$$

For C_m the same procedure applies as in the NTUA case. The downwash corrections are applied to the AoA and the drag coefficient:

$$\alpha' = \alpha + \frac{57.3\delta S}{C} C_L \tag{43}$$

$$C'_D = C'_D + \frac{\delta S}{C} C_L^2 \tag{44}$$

The boundary correction factor δ can be estimated from the literature [9]. Namely, for elliptical load distribution, a rectangular test section with an aspect ratio of approximately 1, and a model span of approximately 0.25 times the jet width, $\delta \approx 0.14$.

2.5 Uncertainties

The presence of uncertainties is inherent in every measurement; therefore it is important to be able to have an estimate of them. Using the framework laid out by JGM [20], we consider uncertainties to be of two types:

- Type A: uncertainties estimated via statistical analysis, e.g. using the standard deviation.
- Type B: uncertainties that are quantified by other means such as calibration certificates etc.

The estimation of Type B uncertainties is achievable only for a part of the measured quantities, as some information may be unavailable between the two facilities. Conversely, the estimation of Type A uncertainties is challenging when the measured signals are non-stationary (e.g. the temperature increases as the WT operates) or the measured behaviour is inherently unsteady (e.g. vortex shedding or separated flow). To alleviate this, a bootstrapping approach was used, taking the average standard deviation of small increments of the signals where Type A uncertainties were evaluated.

Once the uncertainty of each measured quantity is estimated, we can estimate the uncertainties of the derived quantities. To achieve this, assuming that the measurements of different quantities are uncorrelated, the propagation of error can be done using the following formula:

$$\delta u^2 = \sum_{i=1}^{N} \frac{\theta f}{\theta x_i} u^2(x_i) \tag{45}$$

where u is the standard uncertainty of the quantity of interest, calculated as $f\left(x_1, \dots x_N\right)$ with x_i being the i-th independent variable, N the number of independent variables and $u(x_i)$ is the uncertainty of the i-th independent variable.

2.5.1 NTUA

The uncertainties for the NTUA setup are summarized in table 2.

2.5.2 POLIMI

The uncertainties for the POLIMI setup are summarized in table 3.

Table 2: NTUA Uncertainties

Direct Measurements			
Measured Quantity	Measuring Device	Uncertainty Type	Uncertainty (Absolute/Relative)
Freestream Pressure (Pa)	μDAQ2 DTC 32 Channels Pressure Scanner	Type B	6.89 Pa / 0.1% of Full Scale
Freestream Temperature ($^{\circ}C$)	WIKA T91.10.104 Pt100 Thermometer	Type A	0.1°C
Freestream Absolute Pressure (Pa)	Omega OMYL-RH23	Type B	150 Pa
Angle of Attack ($^{\circ}$)	Pulley system attached to a MicroEpsilon Draw-Wire Sensor	Type A	0.2 ($^{\circ}$) / 20% of AoA increments
Surface Pressure (Pa)	μDAQ2 DTC 32 Channels Pressure Scanner	Type B	6.89 Pa / 0.1% of Full Scale
Derived Measurements			
Derived Quantity	Describing Equation	Typical Value	Uncertainty (Absolute/Relative)
Reynolds number	$Re = \frac{cU_\infty}{\nu}$	1.25×10^6	0.5%
Pressure coefficient	$C_p = \frac{p}{q_\infty}$	-3 to 1	$\approx$ 10%
Lift coefficient	eq. (10)	0.21 to 0.7	7% to 3%
Drag coefficient	eq. (11)	0.04 to 0.06	20% to 10%

Table 3: POLIMI Uncertainties

Measured Quantity	Measuring Device	Uncertainty Type	Uncertainty (Absolute/Relative)
Freestream Pressure (Pa)	MENSOR CPT6100 pressure sensor	Type A	≈ 3.5Pa
Freestream Temperature $(^{\circ}C)$	MESCON TH-12U Pt100 Thermometer	Type A	$\approx 0.2^{\circ}$C
Freestream Absolute Pressure	EFFA AK-S 900-1060	Type A	≈ 5Pa
Angle of Attack $(^{\circ})$	Rotary table sensor	Type A	$< 0.1^{\circ}$
Surface Pressure (Pa)	2× ESP-32HD Scanner with DTC	Type B	4.14 Pa / 0.06% of Full Scale
Balance Forces (N & Nm)	RUAG 192-6L Balance	Type B	$\approx (9\text{N}, 12\text{N}, 1.5\text{Nm})$ - $\left(F_x, F_y, M_z\right)$
Derived Measurements			
Derived Quantity	Describing Equation	Typical Value	Uncertainty (Absolute/Relative)
Reynolds number	$Re = \frac{cU_\infty}{\nu}$	1.18×10^6	0.3%
Pressure coefficient	$C_p = \frac{p}{q_\infty}$	-3 to 1	$\approx 5\%$
Lift coefficient (from pressure)	eq. (10)	0.17 to 1.7	6% to 0.6%
Drag coefficient (from pressure)	eq. (11)	0.06 to 0.32	6% to 2.2%
Lift coefficient (from balance)	eq. (12)	0.17 to 1.7	7% to 1.5%
Drag coefficient (from balance)	eq. (13)	0.08 to 0.4	16% to 5.5%

3 Flow control devices design and testing

Three diffrent families of flow control devices, as well as their combinations were tested. Namely, the effect of using Vortex Generators (VGs), Gurney Flaps and TE tabs was investigated.

3.1 Vortex Generators

Vortex Generators (VGs) are small vanes that protrude a wing surface close to its leading edge and generate streamwise vortices that energize the local boundary layer (BL), leading to delayed flow separation and, as a result, increased lift. Typically VGs are placed in arrays at a predefined chordwise position along the span of a wing. The definition of the main geometrical parameters describing an array of VGs is shown in fig. 10. In this Twin Test, VG arrays were 3D printed and the thickness of each VG vane was 0.8mm, a baseplate was also included in the design with beveled edges in order to minimize the disturbance to the flow.

3.1.1 Flow separation

The 'traditional' use of VGs is to delay flow separation and are therefore placed near the maximum thickness of the airfoil. In this Twin Test we placed VGs both at the pressure and suction side of the airfoil, a common practice for very thick airfoils [21]. The VG height h_{VG} was determined in relation to the height of the separating boundary layer (BL), as determined by precursory Computational Fluid Dynamics simulations.

For the suction side VGs, the vane angle was $\beta = 15^\circ$, the distance between consecutive counterrotating VGs $d = 3.5h_{VG}$ and the VG length $L_{VG} = 3h_{VG}$. The distance between consecutive VG pairs is $D/h_{VG} = 7$. Regarding the VG height, initially, the VGs were designed in order to be placed at a chordwise location of $x/c = 40\%$, where $\delta = 0.86\%c$ at 0° and a height of $h_{VG} = 0.8\delta$ was selected. However, during the NTUA campaign, the effect of VGs was minimal and a decision was made to move the array to a more upstream position, namely at $x/ = 30\%$, corresponding to $h_{VG} \approx 1.43\delta$.

Similarly, for the pressure side VGs, $\beta = 15^\circ$, $d = 3.5h_{VG}$, $L_{VG} = 3h_{VG}$ and $D/h_{VG} = 7$. The initial placement was at a chordwise location of $x/c = 55\%$, where $\delta = 1.18\%c$ at 0° and a height of $h_{VG} = 0.8\delta$ was selected. The final position of the arrays was at $x/c = 35\%$, corresponding to corresponding to $h_{VG} \approx 1.48\delta$.

3.1.2 Drag reduction

A different utilization of the streamwise vortices generated by the VGs was considered also here, using said vortices in order to influence the (spanwise) vortices shed from the thick TE of the FB airfoil. The goal is to suppress vortex shedding near the TE, and as a result to increase base pressure and reduce airfoil drag. Different arrays of triangular VGs were placed at the suction side of the airfoil at a streamwise position of $x/c = 90\%$. The VG height h_{VG} was determined in relation to the height of suction side separating BL, as in the case of the VGs for flow separation. Namely, $\delta = 3.84\%c$ at 0° and we selected $h_{VG} = 0.5\delta$; the height of the baseplate (0.6mm) was included in the final height of the VGs. Typical values (see e.g. [22]) were selected for the vane angle $\beta = 15^\circ$, the distance between consecutive counterrotating VGs $d = 2.5h_{VG}$ as well as the VG length $L_{VG} = 3h_{VG}$. Different spanwise distances between consecutive VG pairs D were examined based on the spanwise wavelengths of secondary wake instabilities present in bluff body shedding [23], namely, $D/h_{TE} = (1, 1.4, 2)$, or equivalently $D/h_{VG} = (4.2, 5.85, 8.35)$.

Co-funded by
the European Union

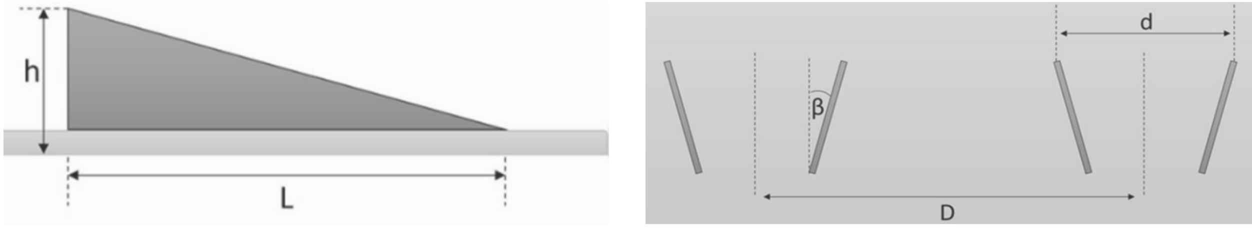

Figure 10: Definition of geometrical parameters of an array of VGs [24].

3.2 Gurney Flaps

Another common flow control solution is the use of Gurney Flaps (GFs), they are thin strips placed normal to the pressure side that are extending the trailing edge of the airfoil. The underlying flow control mechanism is the shift to the Kutta condition via the modification of the circulation around the airfoil, leading to an increase in both lift and drag. The use of GFs has been explored for FB arifoils [21] and wind turbine airfoils in general [25, 26, 24].

Regarding the height, the GF must lie inside the pressure side BL; see e.g. [27, 28]. Due to the large separating BL thickness in thick airfoils, typical values of GF heights are $h_{GF} = 3\%c$ to $7\%c$. In the NTUA tests, three variations of a GF with $h_{GF} = 3\%c$ were used. Namely, a uniform GF and two different segmented variants, one with rectangular and one with triangular [29] segments. The aim of using segmented GFs is based on the idea that by reducing the total area of the GF, the drag induced by it is reduced, while lift stays the same. While in the POLIMI campaign, a uniform GF with $h_{GF} = 5\%c$ made out of a thin metal sheet was used.

3.3 Trailing Edge tabs

Finally, another drag reduction device utilized in the Twin Test were small tabs placed near the in the pressure side of the airfoil. The concept of TE tabs was firstly discussed by [30]. The underlying mechanism the mean-velocity modification along the spanwise direction, i.e. deceleration and acceleration of the mean streamwise velocity near and away from the tab, respectively. This mean-velocity distribution along the spanwise direction causes the spanwise mismatch in the vortex-shedding process and eventually results in vortex dislocation in the wake [30]. For the WT tests, arrays of tabs were 3D-printed. Each tab was 2.5mm thick, while the height of each tab was $l_y/h_{TE} = 0.1$ and their width along the span was $l_z/h_{TE} = 0.25$. Regarding the spanwise distance between consecutive tabs λ, three different configurations were tested $\lambda/h_{TE} = 1, 1.5, 2$

Additionally, combinations of the previously desicribed flow control options were also investigated. In fig. 11 the airfoil model with some of the tested flow control options is shown. Namely the VG arrays for flow separation control are placed in both the pressure and suction sides. Addtionally, in the suction side (left hand side of the TE) the array of VGs designed for drag reduction is visible in black. Finally, the TE tabs extending in the pressure side of the TE (right hand side) are shown in brown.

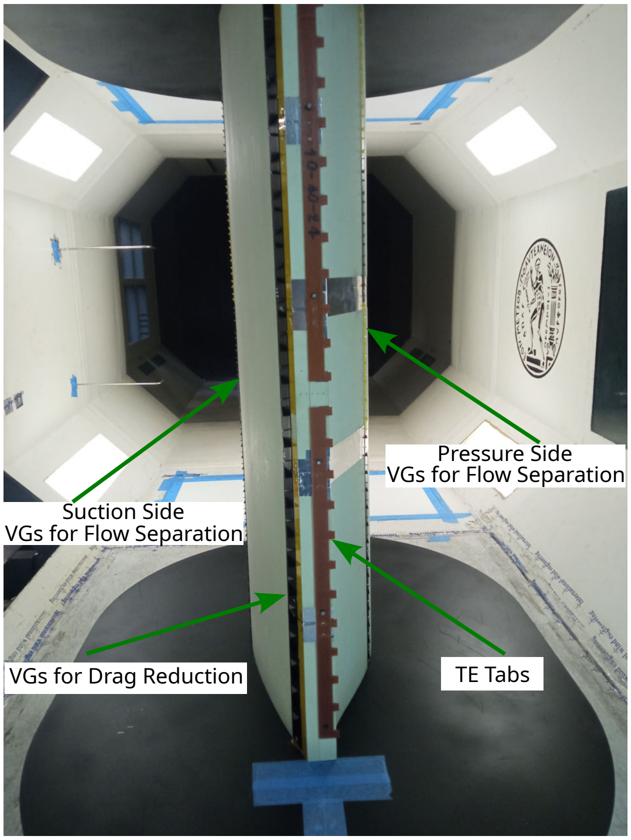

Figure 11: The model installed in the NTUA WT with a combination of flow control devices. View of the model trailing edge looking upstream.

Co-funded by
the European Union

4 Results

In this section we present the results for the two campaigns and it is organized as follows. First the baseline is established for both the free and fixed transition cases. Next, the effect of the designed and tested flow control devices is demonstrated. Namely, the improvement in flow separation behaviour introduced by placing VGs near the maximum thickness of the airfoil is highlighted. Additonally, we show the effectiveness of drag reduction achieved by the concept of placing VGs near the TE, as well as tabs placed near the TE. Furthermore, the lift increase introduced by the use of GFs is presented. Finally, the combination of GFs and TE VGs is shown.

4.1 Baseline - Free BL transition

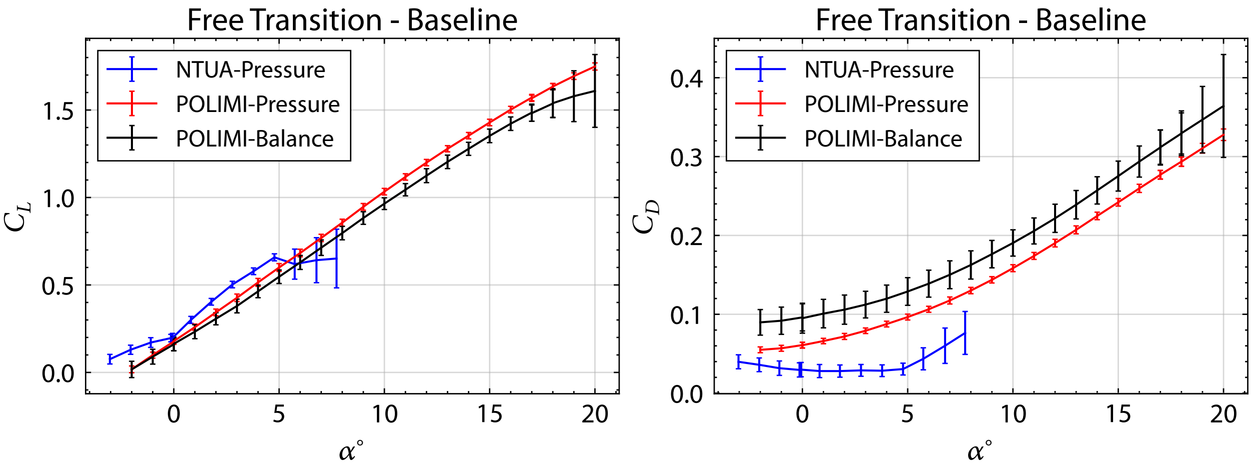

(a) (b)

Figure 12: Polars for the baseline case with free BL transition (a) C_L (b) C_D.

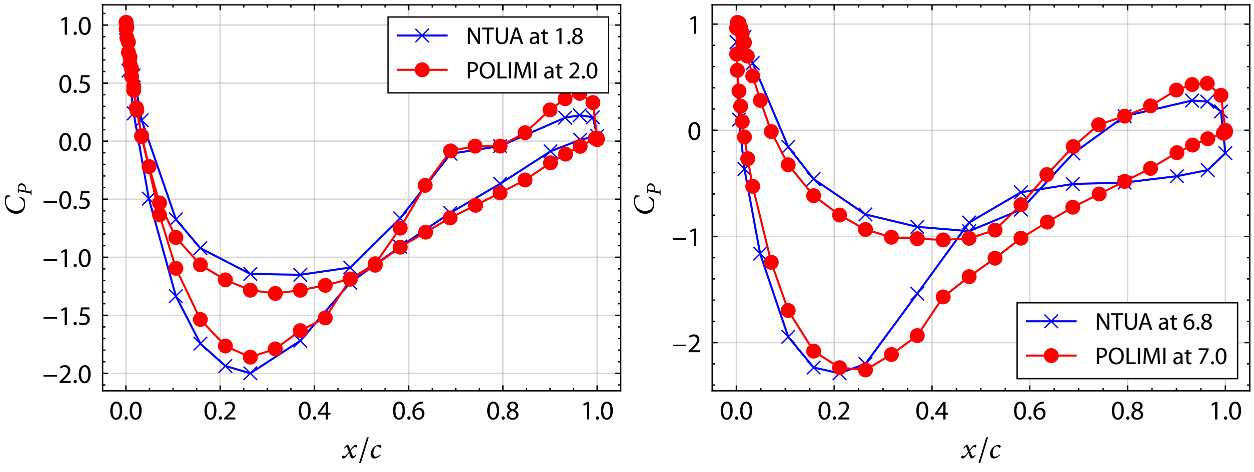

(a)

(b)

Figure 13: Pressure coefficient C_p distribution around the airfoil at (a) $\alpha = 2^\circ$ and (b) $\alpha = 6^\circ$ for the baseline case with free BL transition (a) C_L (b) C_D.

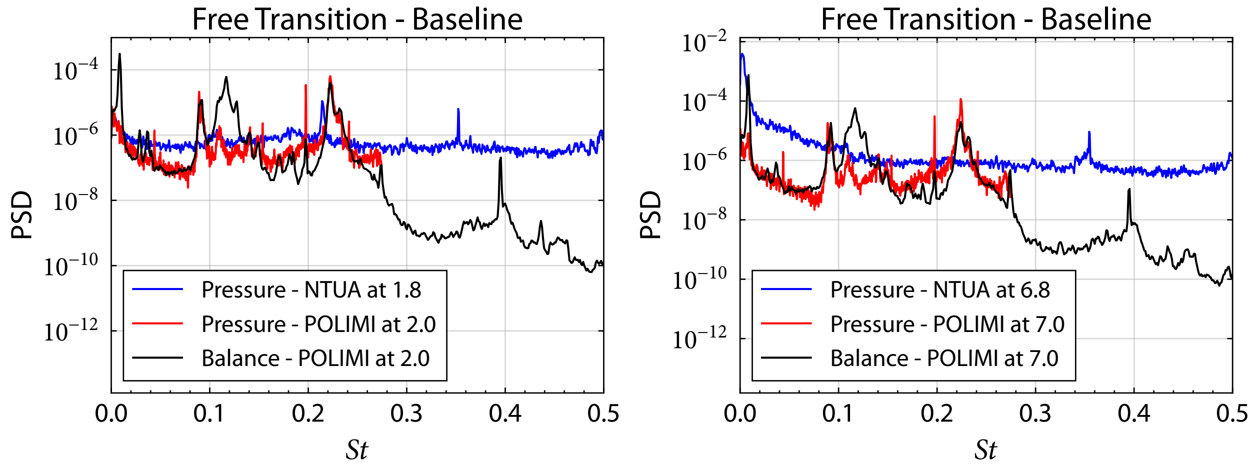

(a)

(b)

Figure 14: Spectral behaviour of C_L at (a) $\alpha = 2^\circ$ (b) $\alpha = 6^\circ$ for the baseline case with fixed BL transition.

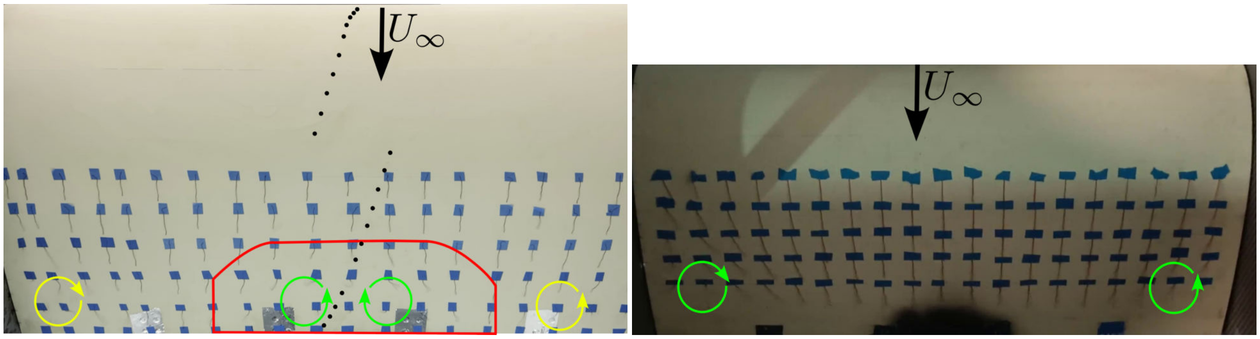

(a) (b)

Figure 15: Surface flow vizualisation with tufts for (a) NTUA at $\alpha = 6^\circ$ (b) POLIMI at $\alpha = 18^\circ$.

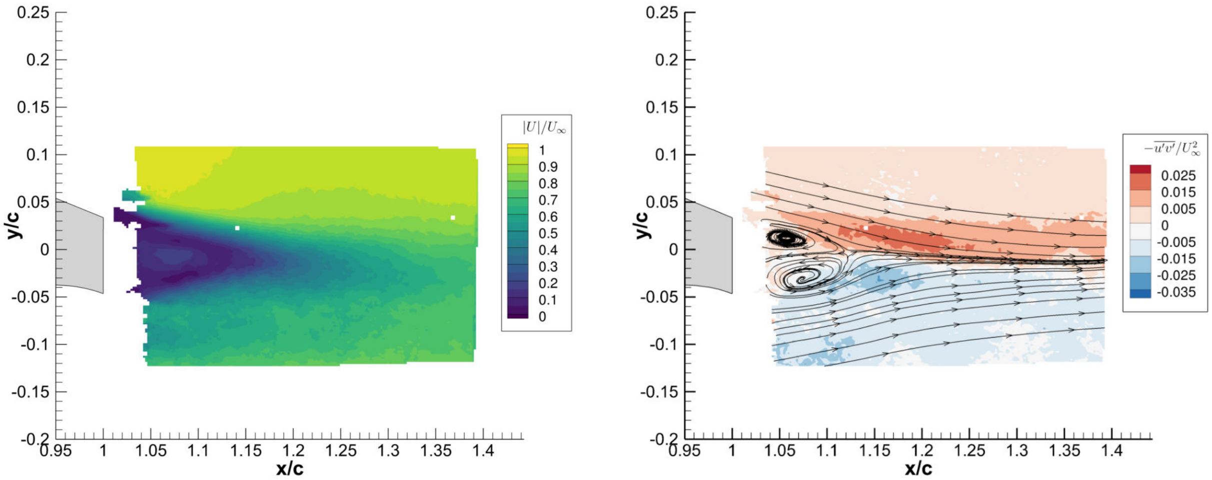

(a) (b)

Figure 16: Stereo PIV results for the baseline case with free BL transition at $\alpha - 0.3^\circ$(a) normalized velocity magnitude $|U|/U_\infty$ and (b) normalized Reynolds stress $-\overline{u'v'}/U_\infty^2$ contours.

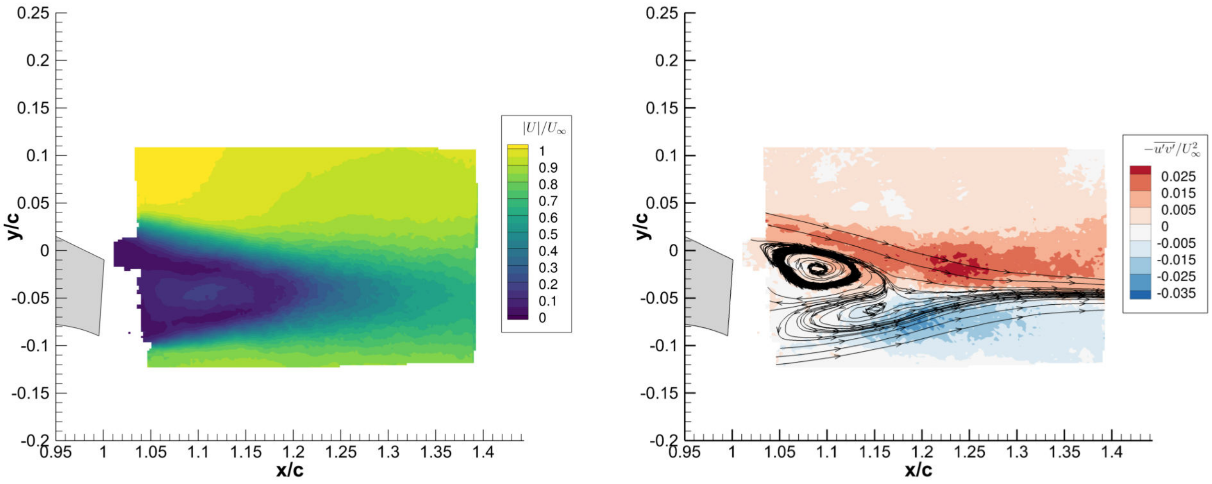

(a)

(b)

Figure 17: Stereo PIV results for the baseline case with free BL transition at $\alpha 3.9^\circ$(a) normalized velocity magnitude $|U|/U_\infty$ and (b) normalized Reynolds stress $-\overline{u'v'}/U_\infty^2$ contours.

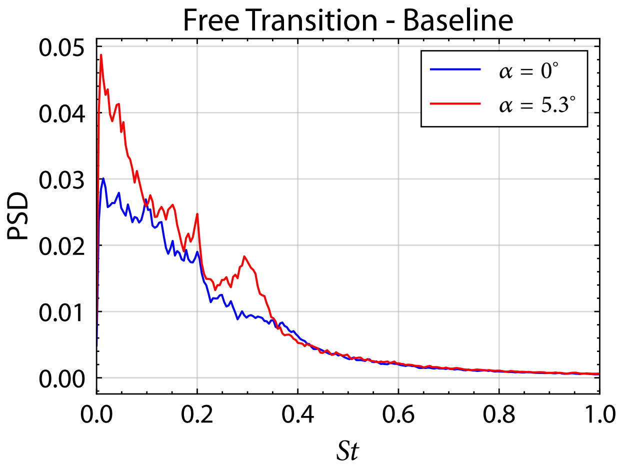

Figure 18: Power Spectral Density for the hot-wire measurements taken at NTUA for two AoAs. Baseline case with free BL transition

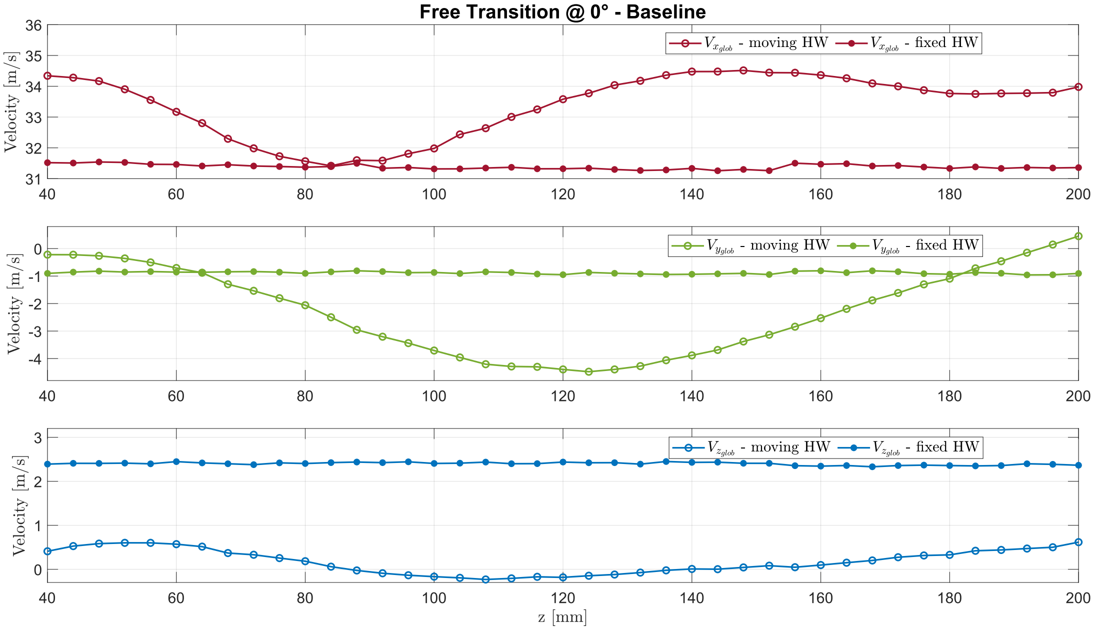

Figure 19: Distribution of mean value of each velocity component along the span measured via hot-wires in POLIMI for free BL transition.

4.2 Baseline - Fixed BL transition

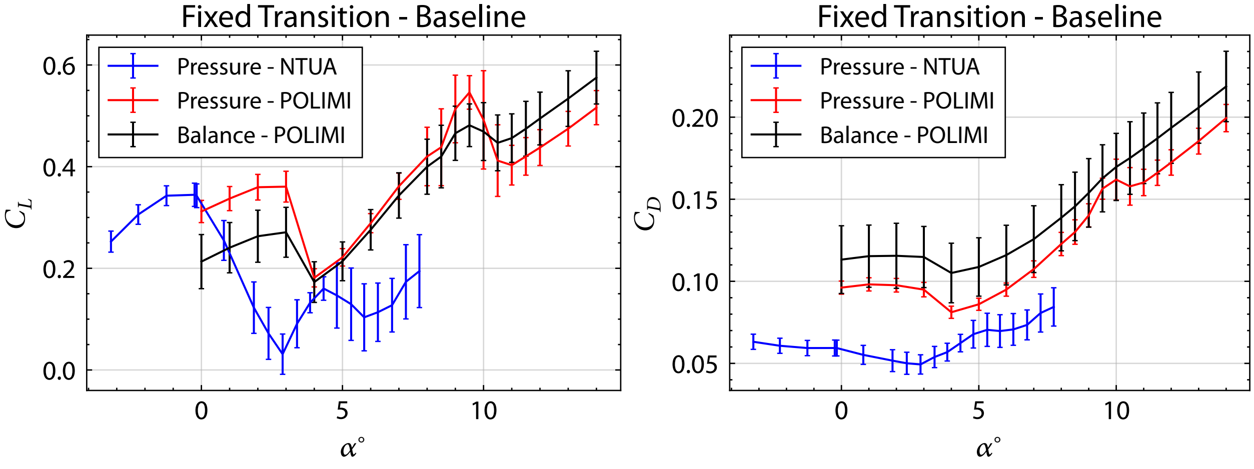

(a)

(b)

Figure 20: Polars for the baseline case with fixed BL transition (a) C_L (b) C_D.

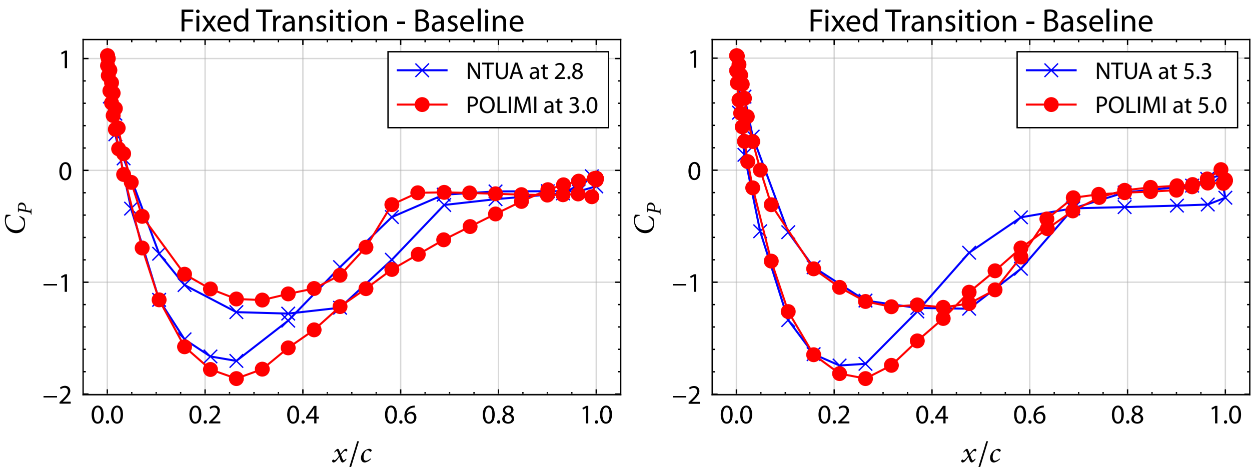

(a)

(b)

Figure 21: Pressure coefficient C_p distribution around the airfoil at (a) $\alpha = 3^\circ$ and (b) $\alpha = 5^\circ$ for the baseline case with fixed BL transition (a) C_L (b) C_D.

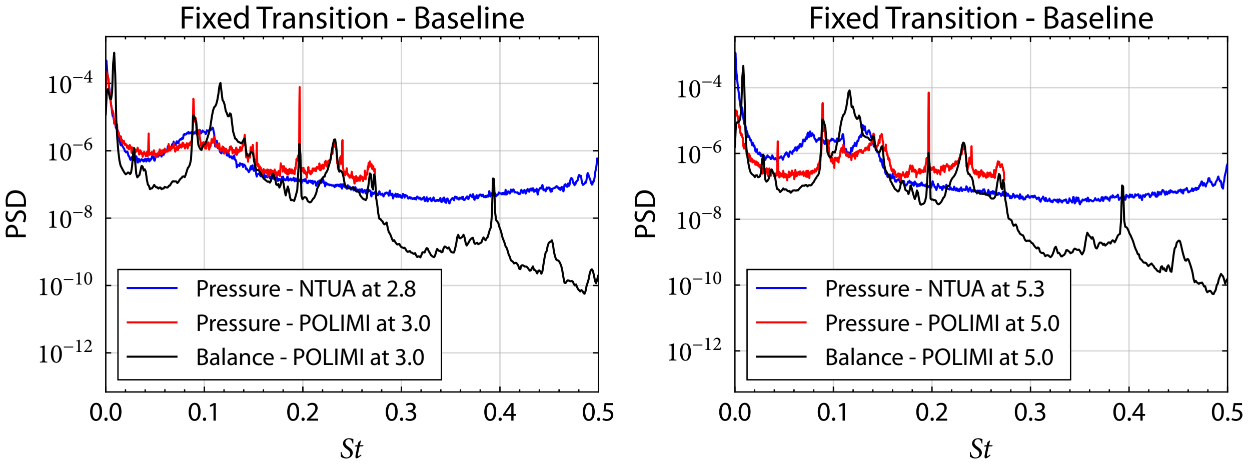

(a)

(b)

Figure 22: Spectral behaviour of C_L at (a) $\alpha = 3^\circ$ (b) $\alpha = 5^\circ$ for the baseline case with fixed BL transition.

Co-funded by
the European Union

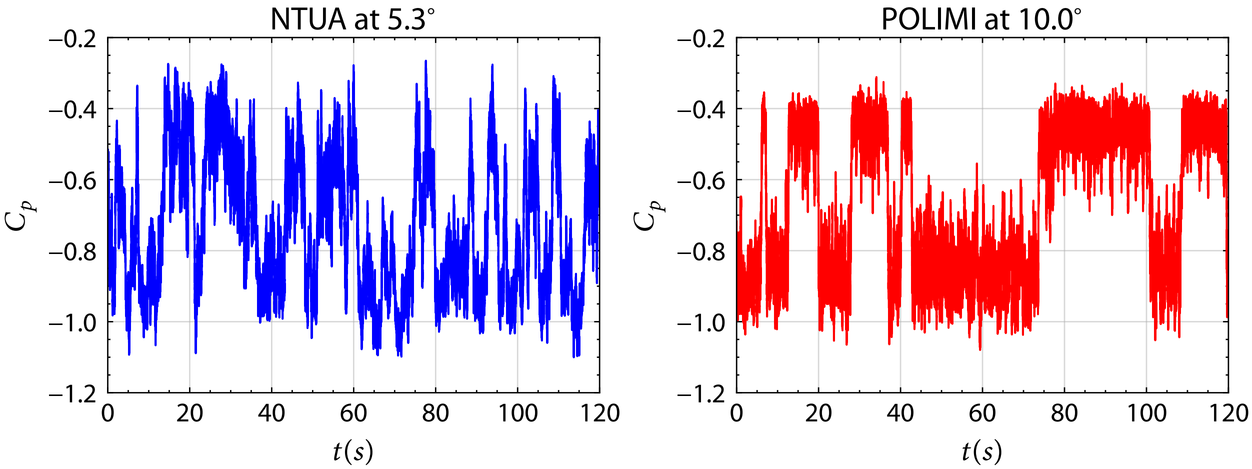

(a)

(b)

Figure 23: Timeseries of C_p at the tap located at $x/c = 0.48$ and $y/c = 0.2$ for the AoAs demonstrating bifurcating behaviour for the fixed BL transition at (a) NTUA (b) POLIMI.

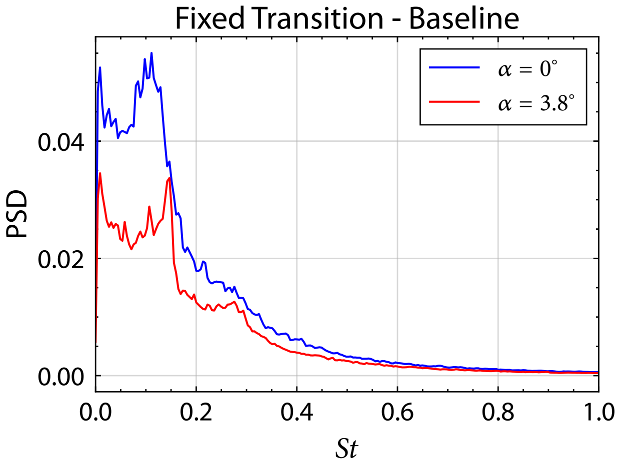

Figure 24: Power Spectral Density for the hot-wire measurements taken at NTUA for two AoAs. Baseline case with fixed BL transition.

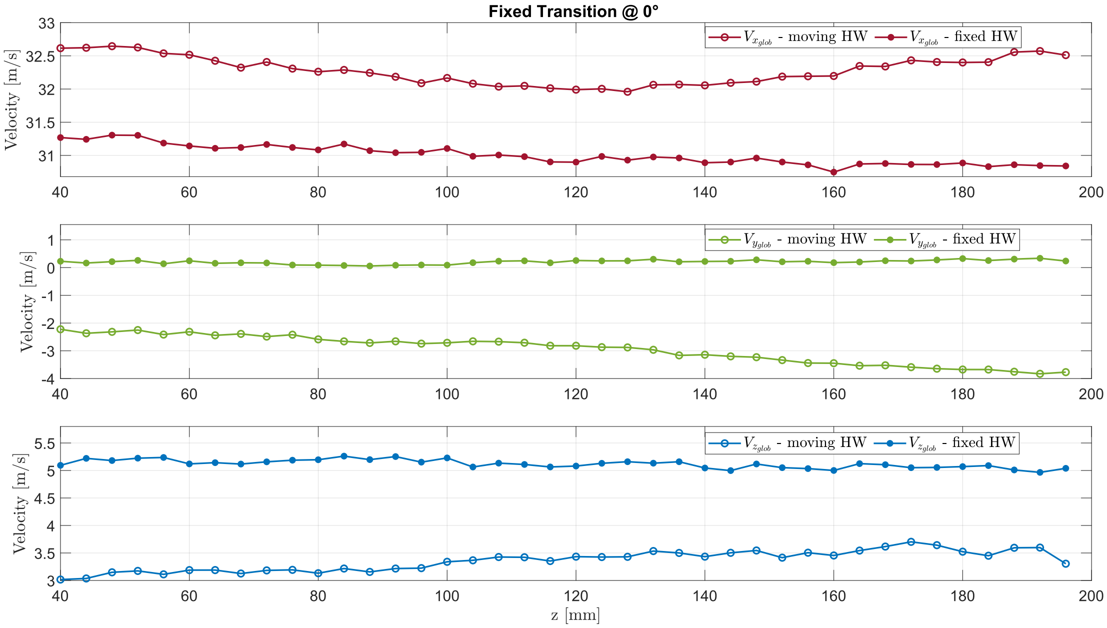

Figure 25: Distribution of mean value of each velocity component along the span measured via hot-wires in POLIMI for fixed BL transition.

4.3 Flow Control

4.3.1 VGs for flow separation

4.3.1.1 Performance of VGs

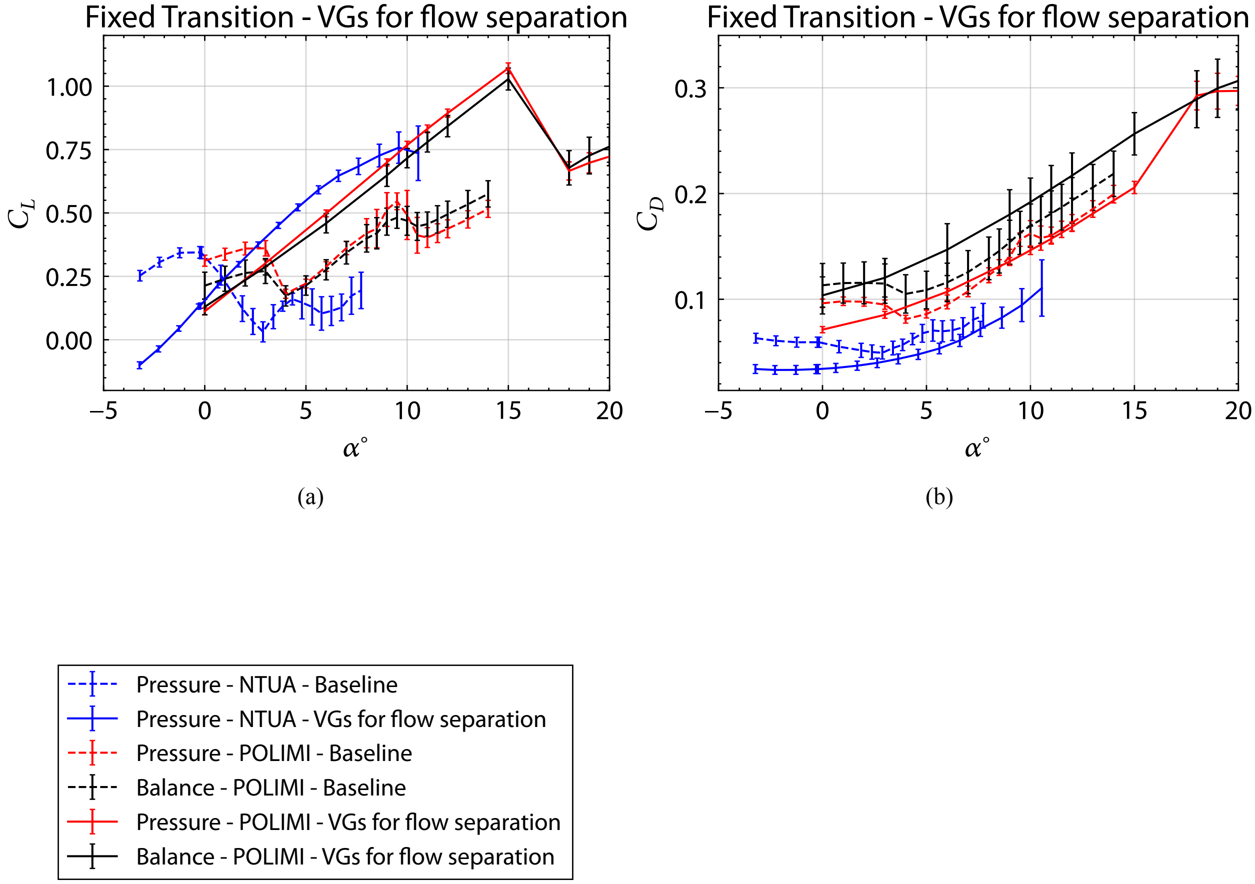

(a)

(b)

(c)

Figure 26: Polars for the case with VGs for flow separation control and fixed BL transition (a) C_L, (b) C_D, (c) Legend.

4.3.1.2 Effect of BL transition

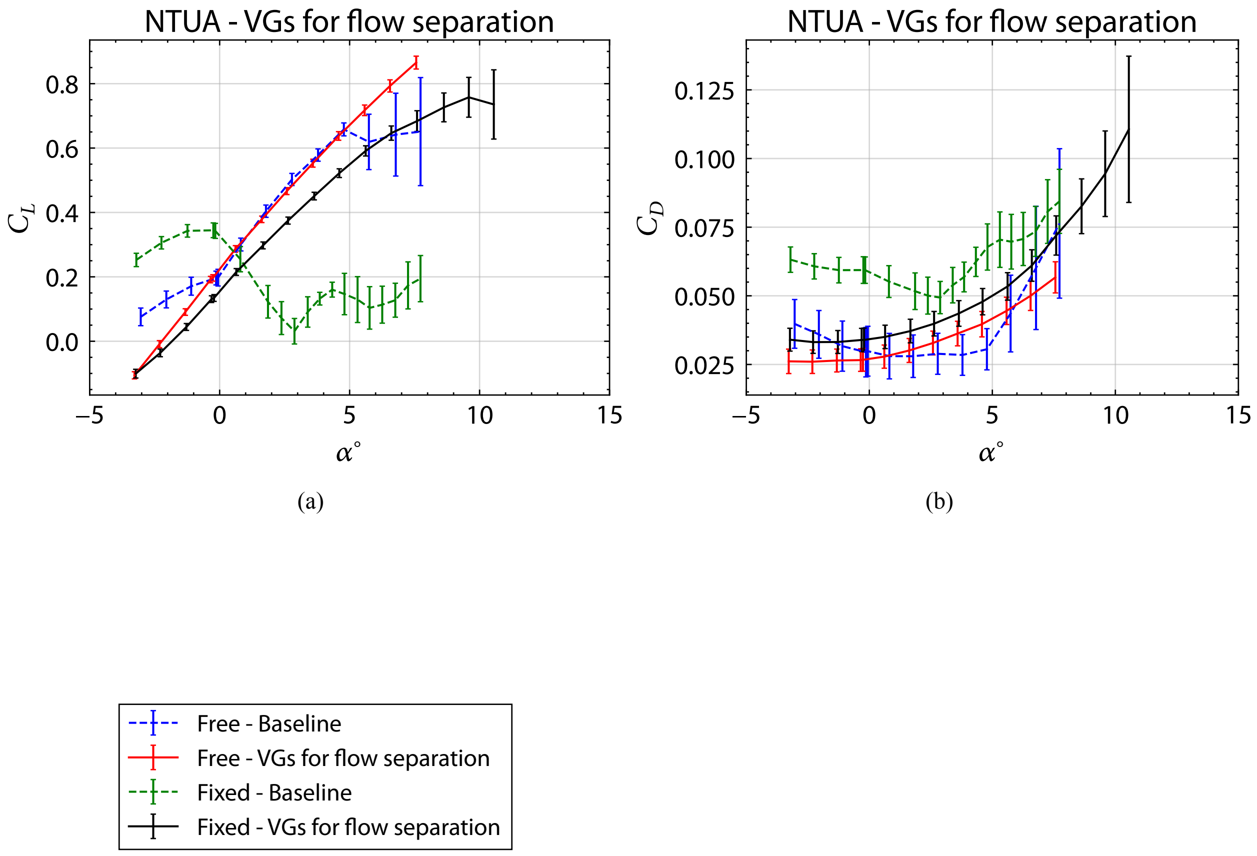

(a)

(b)

(c)

Figure 27: NTUA results for the case with VGs for flow separation control (a) C_L, (b) C_D, (c) Legend.

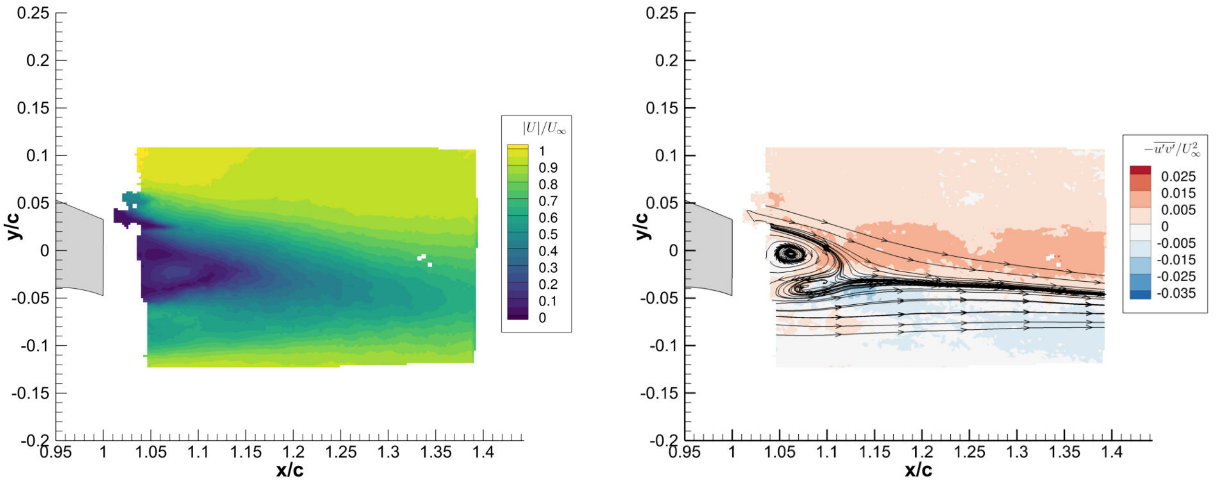

(a) (b)

Figure 28: Stereo PIV results for the case with VGs for flow separation control and free BL transition at $\alpha 0.1^\circ$(a) normalized velocity magnitude $|U|/U_\infty$ and (b) normalized Reynolds stress $-\overline{u'v'}/U_\infty^2$ contours.

4.3.1.3 Bifurcation observed in POLIMI

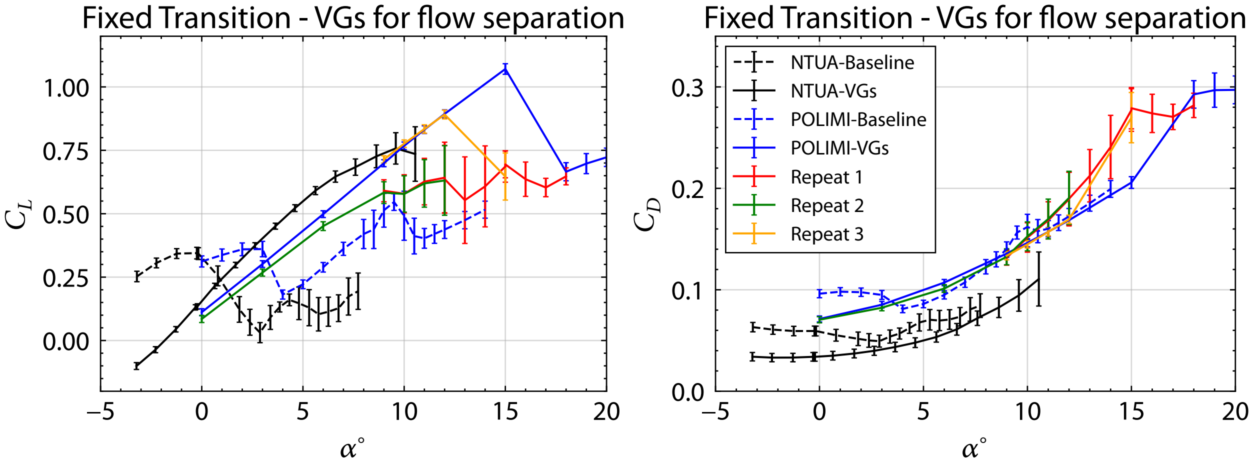

(a) (b)

Figure 29: Polars only from surface pressure measurements for the case with VGs for flow separation control and fixed BL transition (a) C_L (b) C_D.

4.3.2 VGs for drag reduction

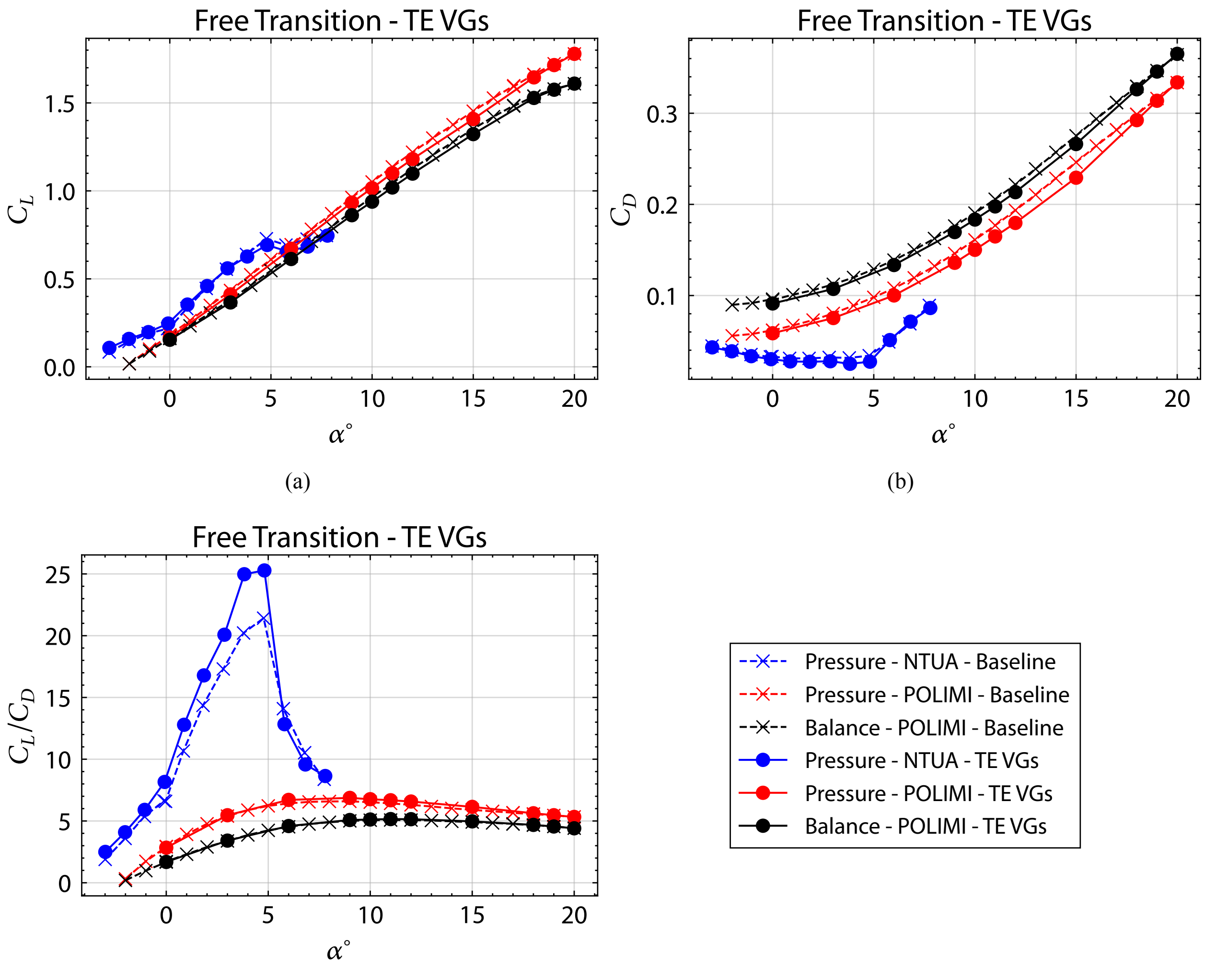

(a) (b)

(c) (d)

Figure 30: Polars for the case with VGs for drag reduction and free BL transition (a) C_L, (b) C_D, (c) C_L/C_D (d) Legend.

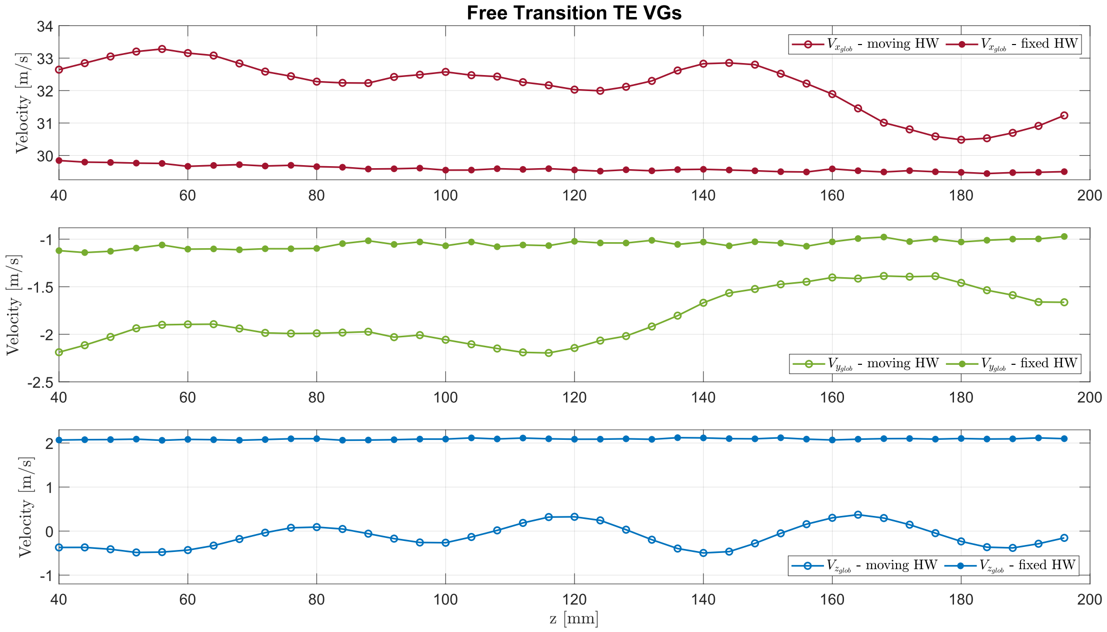

Figure 31: Distribution of mean value of each velocity component along the span measured via hot-wires in POLIMI for free BL transition and VGs placed at $x/c = 0.9$ on the suction side.

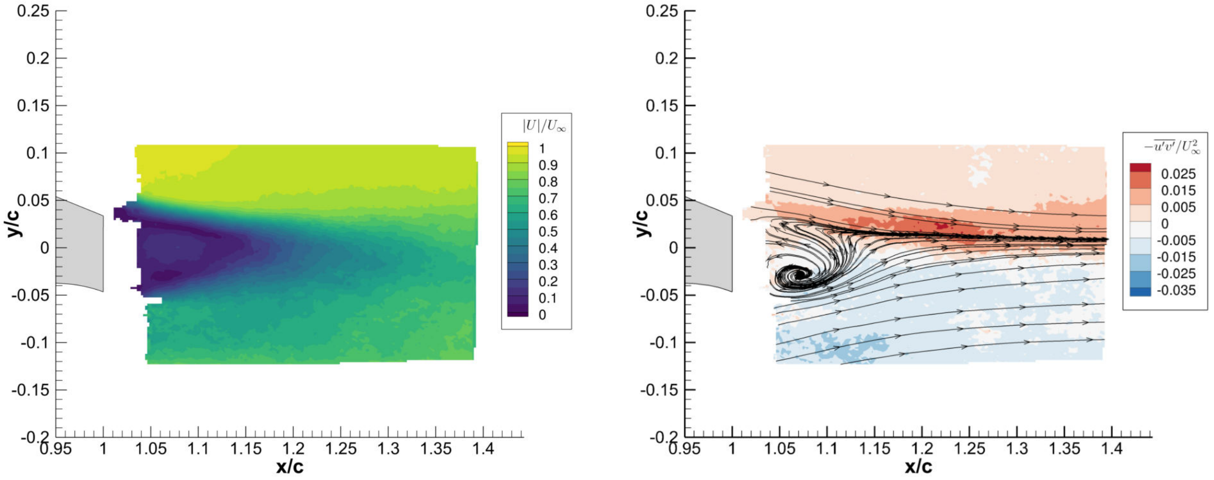

(a)

(b)

Figure 32: Stereo PIV results for the case with VGs for drag reduction and free BL transition at $\alpha 0°$(a) normalized velocity magnitude $|U|/U_\infty$ and (b) normalized Reynolds stress $-\overline{u'v'}/U_\infty^2$ contours.

4.3.3 TE tabs

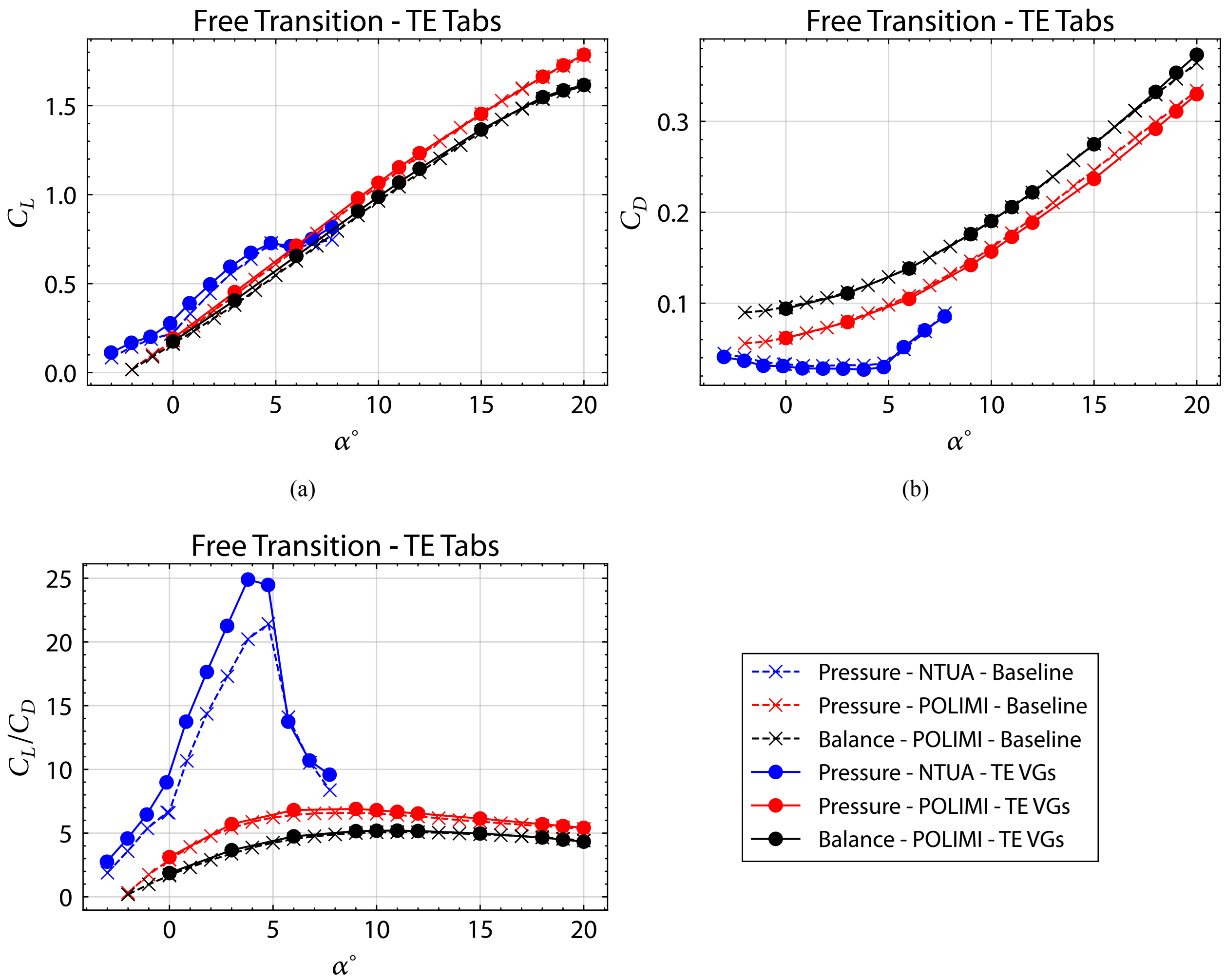

(a)

(b)

(c)

(d)

Figure 33: Polars for the case with TE tabs and free BL transition (a) C_L, (b) C_D, (c) C_L/C_D.

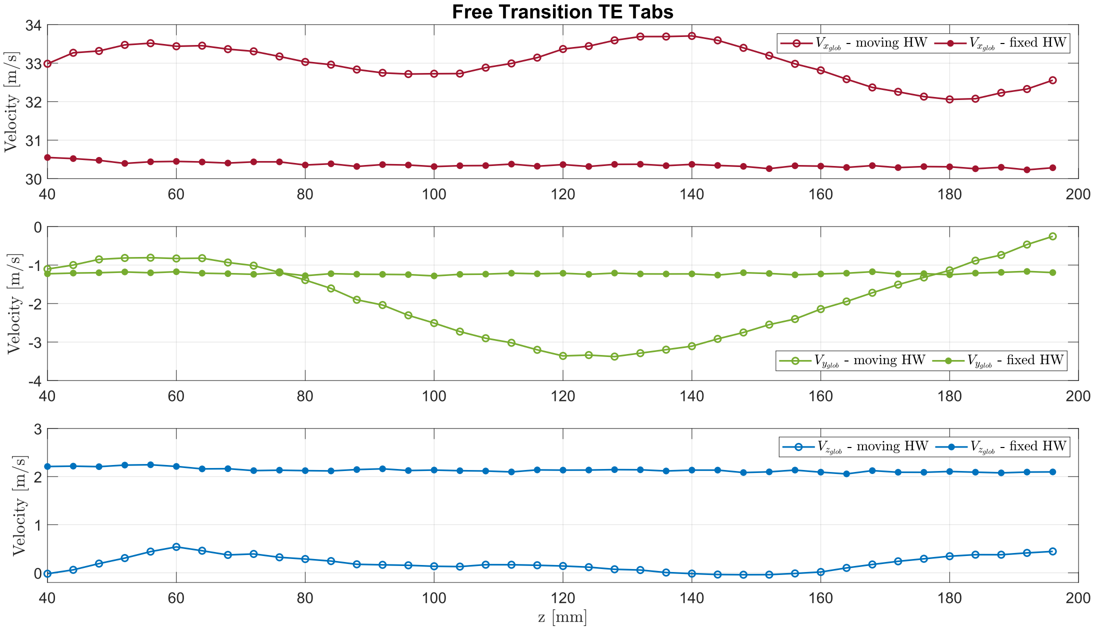

Figure 34: Distribution of mean value of each velocity component along the span measured via hot-wires in POLIMI for free BL transition and using TE tabs.

4.3.4 Gurney Flaps

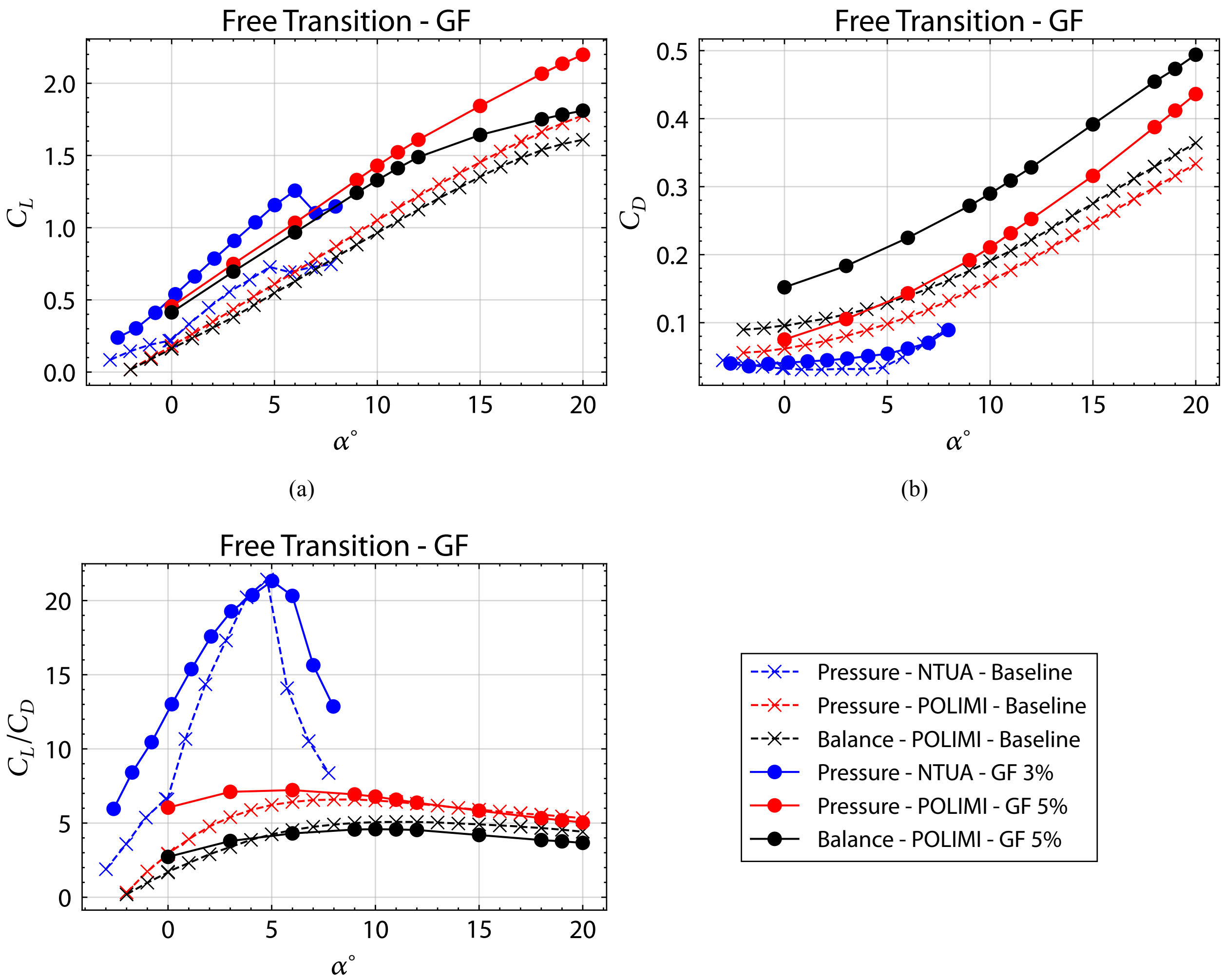

(a) (b)

(c) (d)

Figure 35: Polars for the case with Gurney flaps and free BL transition (a) C_L, (b) C_D, (c) C_L/C_D.

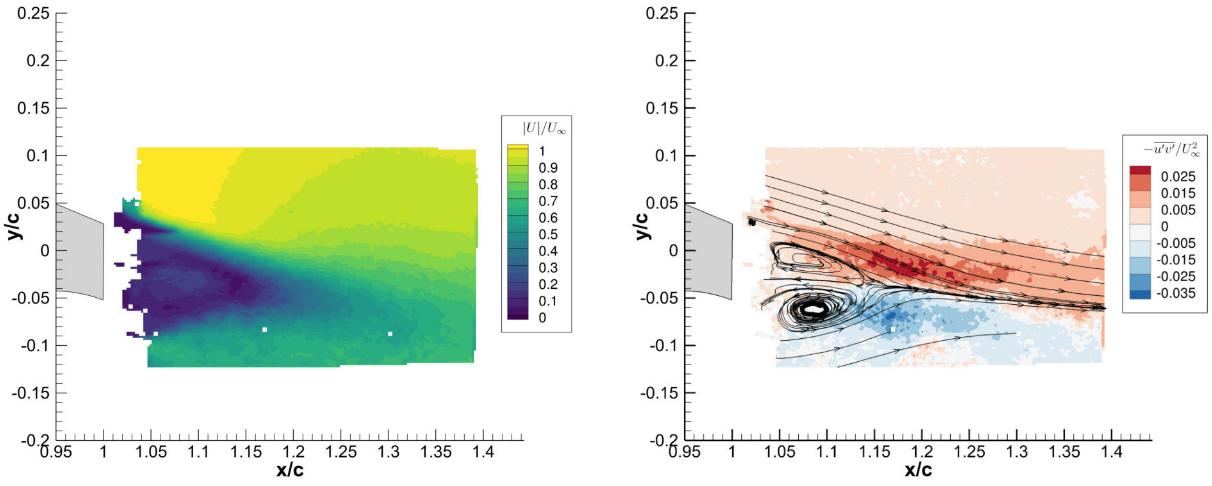

(a) (b)

Figure 36: Stereo PIV results for the case with Gurney flaps and free BL transition at $\alpha 0.5°$(a) normalized velocity magnitude $|U|/U_\infty$ and (b) normalized Reynolds stress $-\overline{u'v'}/U_\infty^2$ contours.

Co-funded by the European Union

4.3.5 Gurney Flaps & VGs for drag reduction

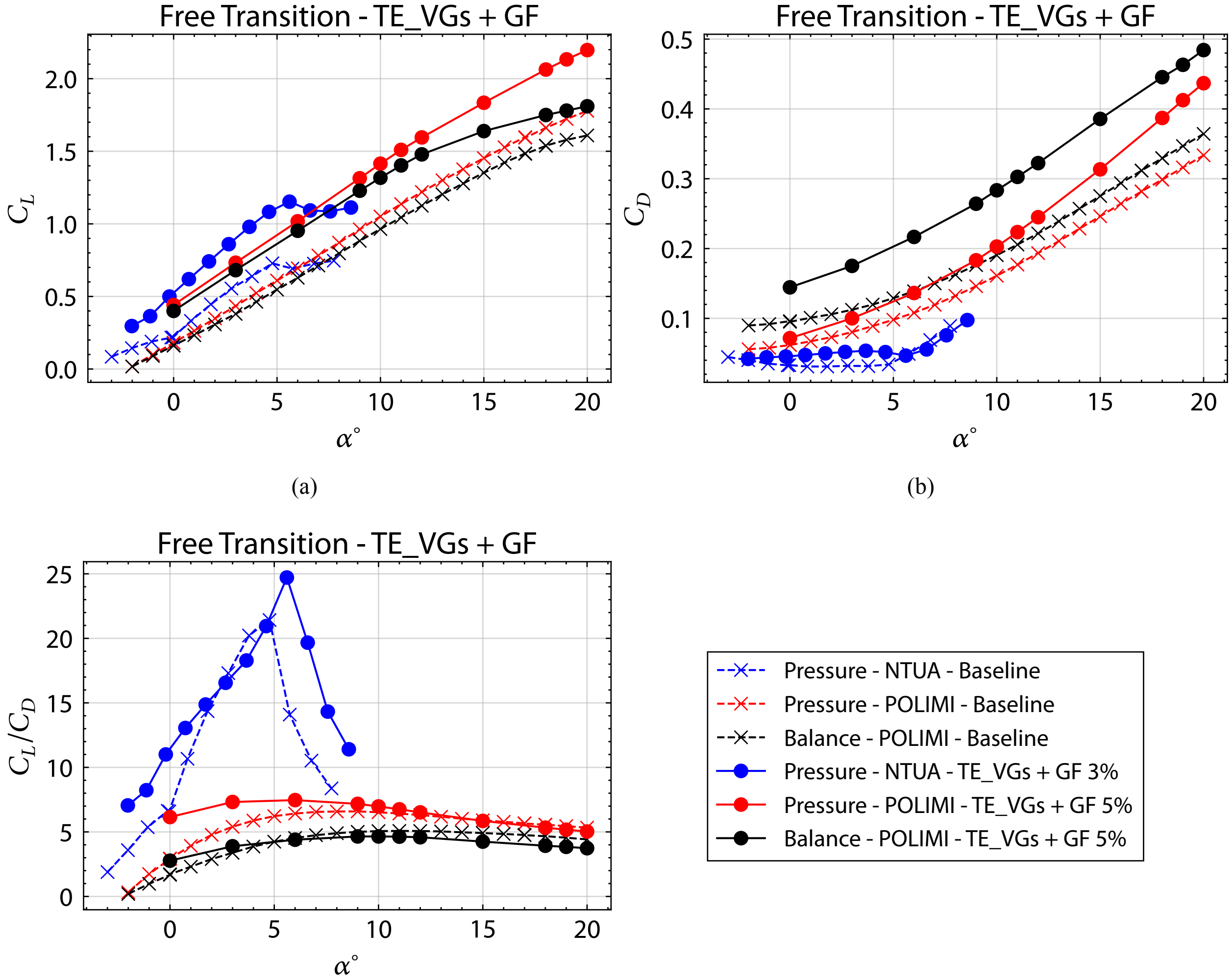

(a)

(b)

(c)

(d)

Figure 37: Polars for the case with VGs for drag reduction and GF for free BL transition (a) C_L, (b) C_D, (c) C_L/C_D (d) Legend.

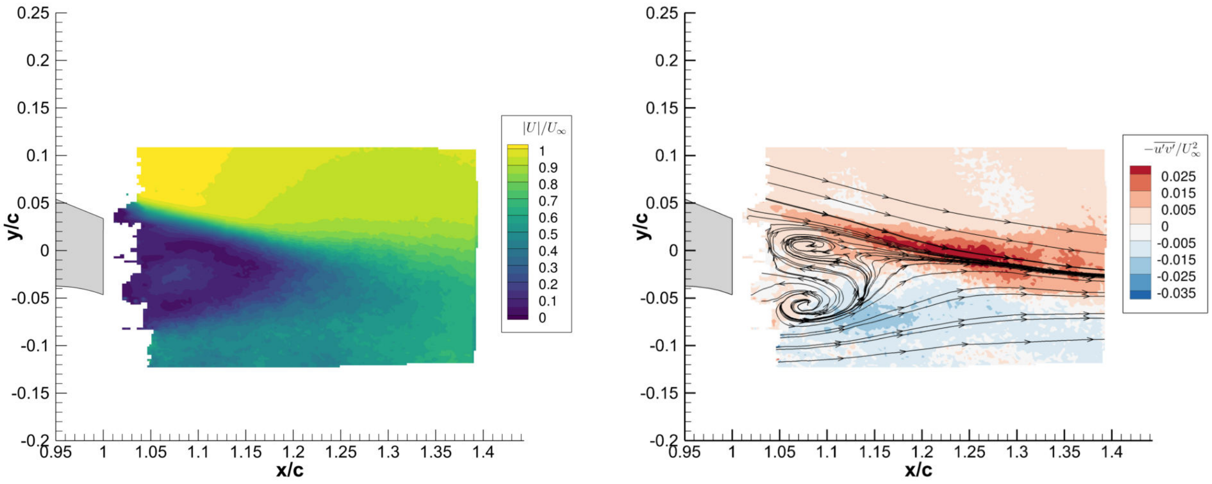

(a)

(b)

Figure 38: Stereo PIV results for the case with VGs for drag reduction and GF and free BL transition at $\alpha 0^\circ$(a) normalized velocity magnitude $|U|/U_\infty$ and (b) normalized Reynolds stress $-\overline{u'v'}/U_\infty^2$ contours.

5 Summary

This chapter presented the facilities, equipment and set up details for the two campaigns carried out in the wind tunnels of the National Technical University of Athens (NTUA) and Politecnico di Milano (POLIMI) within the scope of Twin Test 3 of the TWEET-IE project. Namely, Twin Tests were conducted assessing the effect of micro devices for enhanced performance of flatback airfoil sections. The utter goal was to investigate the effect of freestream turbulence intensity, Reynolds number and blockage ratio on airfoil performance, 3D flow separation and wake behaviour. Additionally, the effect of flow control devices regarding flow separation control and drag reduction were assessed. The results between the two facilities deviate significantly even at the baseline case, which at this stage is attributed to 3D separated flow and differences in blockage. For the fixed BL transition case, force and pressure timeseries demonstrate a switching behaviour between intermittent states, in both facilities but at different rangers of AoAs and at different timescales. The use of VGs for flow separation control has a positive effect in both facilities. Additionally, using a Gurney flap leads to an increase in lift force (almost doubling it), but it comes with an increase in drag at both facilities, leading to small aerodynamic performance gains, especially at low AoAs. Finally, the effectiveness of placing drag reduction devices at or near the TE (VGs and tabs) varies between facilities. Namely, at NTUA the aerodynamic performance is increased in a similar way for the TE VGs and TE tabs, (25%), while the improvement is marginal (approximately 1%) for the POLIMI tests.

References

[1] J. P. Baker, E. A. Mayda, and C. P. Van Dam. “Experimental Analysis of Thick Blunt Trailing-Edge Wind Turbine Airfoils”. In: *Journal of Solar Energy Engineering* 128.4 (Nov. 1, 2006), pp. 422–431. ISSN: 0199-6231, 1528-8986. DOI: `10.1115/1.2346701`.

[2] Daniel Griffith and Phillip Richards. *The SNL100-03 Blade: Design Studies with Flatback Airfoils for the Sandia 100-Meter Blade.* SAND2014-18129, 1159116, 537751. Sandia National Lab, Albuquerque, NM (United States), Sept. 1, 2014, SAND2014–18129, 1159116, 537751.

[3] Matthew Franklin Barone et al. *Aerodynamic and Aeroacoustic Tests of a Flatback Version of the DU97-W-300 Airfoil*. SAND–2009-4185, 1504612. Aug. 1, 2009, SAND–2009-4185, 1504612. DOI: `10.2172/1504612`.

[4] Aubryn Cooperman et al. “Aerodynamic Performance of Thick Blunt Trailing Edge Airfoils”. In: *28th AIAA Applied Aerodynamics Conference*. 28th AIAA Applied Aerodynamics Conference. Chicago, Illinois: American Institute of Aeronautics and Astronautics, June 28, 2010. ISBN: 978-1-62410-141-0. DOI: `10.2514/6.2010-4228`.

[5] Marinos Manolesos and Spyros G. Voutsinas. “Experimental Study of Drag-Reduction Devices on a Flatback Airfoil”. In: *AIAA Journal* 54.11 (Nov. 2016), pp. 3382–3396. DOI: `10.2514/1.j054901`.

[6] Camille N. Metzinger et al. “Experimental and Computational Investigation of Blunt Trailing-Edge Airfoils with Splitter Plates”. In: *AIAA Journal* 56.8 (Aug. 2018), pp. 3229–3239. ISSN: 0001-1452, 1533-385X. DOI: `10.2514/1.J056098`.

[7] *Facility*. NTUA Wind Tunnel. URL: `http://wt.fluid.mech.ntua.gr/` (visited on 09/15/2025).

[8] *Facility*. GVPM Polimi. URL: `https://www.windtunnel.polimi.it/facility/` (visited on 09/15/2025).

[9] Jewel B. Barlow, William H. Rae, and Alan Pope. *Low-Speed Wind Tunnel Testing*. 3. ed. New York Weinheim: Wiley, 1999. 713 pp. ISBN: 978-0-471-55774-6.

[10] John D. Anderson. *Fundamentals of Aerodynamics*. Sixth edition. McGraw-Hill Series in Aeronautical and Aerospace Engineering. New York, NY: McGraw Hill Education, 2017. 1130 pp. ISBN: 978-1-259-12991-9.

[11] H. Bergh and H. Tijdeman. *Theoretical and Experimental Results for the Dynamic Response of Pressure Measuring Systems*. NLR-TR F.238. National Aerospace Laboratory NLR, Jan. 31, 1965.

[12] Stephen A. Whitmore and Matthew D. Wilson. “Wiener Deconvolution for Reconstruction of Pneumatically Attenuated Pressure Signals”. In: *AIAA Journal* 49.5 (May 2011), pp. 890–897. ISSN: 0001-1452, 1533-385X. DOI: `10.2514/1.J050102`.

[13] Norbert Wiener. *Extrapolation, Interpolation, and Smoothing of Stationary Time Series*. Cambridge, MA: MIT Press, 1949.

[14] Tuan-Kiet La and Soon-Duck Kwon. “Reducing Ambient Sensor Noise in Wind Tunnel Tests Using Spectral Subtraction Method”. In: *Journal of Wind Engineering and Industrial Aerodynamics* 244 (Jan. 1, 2024), p. 105631. ISSN: 0167-6105. DOI: `10.1016/j.jweia.2023.105631`.

[15] H. Julian Allen and Walter G. Vincenti. *Wall Interference in a Two-Dimensional-Flow Wind Tunnel, with Consideration of the Effect of Compressibility*. NACA 782. Jan. 1, 1944.

[16] H. C. Garner et al. *Subsonic Wind Tunnel Wall Corrections*. AGARDograph 109. North Atlantic Treaty Organization Advisory Group for Aerospace Research and Development, Oct. 1966.

[17] Sylvain Mouton, Alois Peter Schaffarczyk, and Nando Timmer. “Wind Tunnel Tests of a Thick Wind Turbine Airfoil”. In: *Wind Energy* 27.10 (2024), pp. 994–1010. ISSN: 1099-1824. DOI: `10.1002/we.2938`.

[18] J. E. Hackett and K. R. Cooper. “Extensions to Maskell’s Theory for Blockage Effects on Bluff Bodies in a Closed Wind Tunnel”. In: *The Aeronautical Journal* 105.1050 (Aug. 2001), pp. 409–418. ISSN: 0001-9240, 2059-6464. DOI: `10.1017/S0001924000012380`.

[19] E. C. Maskell. “A Theory of the Blockage Effects on Bluff Bodies and Stalled Wings in a Closed Wind Tunnel”. In: (1963).

[20] BIPM, IEC, IFCC, ILAC, ISO, IUPAC, IUPAP, OIML. *Evaluation of Measurement Data — Guide to the Expression of Uncertainty in Measurement*. Joint Committee for Guides in Metrology, JCGM JCGM 100:2008. 2008. DOI: `10.59161/JCGM100-2008E`.

[21] Antonios Cene, Marinos Manolesos, and Francesco Grasso. “Aerodynamic and Aeroacoustic Measurements of the Flow Past a Very Thick Flatback Airfoil with Passive Flow Control Devices”. In: *AIAA SCITECH 2022 Forum*. AIAA SciTech Forum. American Institute of Aeronautics and Astronautics, Dec. 29, 2021. DOI: `10.2514/6.2022-0279`.

[22] Daniel Baldacchino et al. “Experimental Parameter Study for Passive Vortex Generators on a 30% Thick Airfoil”. In: *Wind Energy* 21.9 (2018), pp. 745–765. ISSN: 1099-1824. DOI: `10.1002/we.2191`.

[23] Bradley Gibeau and Sina Ghaemi. “The Mode B Structure of Streamwise Vortices in the Wake of a Two-Dimensional Blunt Trailing Edge”. In: *Journal of Fluid Mechanics* 884 (Feb. 10, 2020), A12. ISSN: 0022-1120, 1469-7645. DOI: `10.1017/jfm.2019.931`.

[24] L Chng et al. “On the Combined Use of Vortex Generators and Gurney Flaps for Turbine Airfoils”. In: *Journal of Physics: Conference Series* 2265.3 (May 1, 2022), p. 032040. ISSN: 1742-6588, 1742-6596. DOI: `10.1088/1742-6596/2265/3/032040`.

[25] Joerg Alber et al. “Parametric Investigation of Gurney Flaps for the Use on Wind Turbine Blades”. In: *Volume 9: Oil and Gas Applications; Supercritical CO2 Power Cycles; Wind Energy*. ASME Turbo Expo 2017: Turbomachinery Technical Conference and Exposition. Charlotte, North Carolina, USA: American Society of Mechanical Engineers, June 26, 2017, V009T49A015. ISBN: 978-0-7918-5096-1. DOI: `10.1115/GT2017-64475`.

[26] Jörg Alber et al. “Experimental Investigation of Mini Gurney Flaps in Combination with Vortex Generators for Improved Wind Turbine Blade Performance”. In: *Wind Energy Science* 7.3 (May 3, 2022), pp. 943–965. ISSN: 2366-7451. DOI: `10.5194/wes-7-943-2022`.

[27] Philippe Giguere, Guy Dumas, and Jean Lemay. “Gurney Flap Scaling for Optimum Lift-to-Drag Ratio”. In: *AIAA Journal* 35.12 (1997), pp. 1888–1890. ISSN: 0001-1452. DOI: `10.2514/2.49`.

[28] Benoît Genest and Guy Dumas. “Numerical Investigation into Single and Double Gurney Flaps for Improving Airfoil Performance”. In: *Journal of Aircraft* 60.6 (Nov. 2023), pp. 1832–1846. ISSN: 0021-8669, 1533-3868. DOI: `10.2514/1.C037304`.

[29] Xuemin Ye et al. “Numerical Study on Aerodynamic Performance and Noise of Wind Turbine Airfoils with Serrated Gurney Flap”. In: *Energy* 262 (Jan. 1, 2023), p. 125574. ISSN: 0360-5442. DOI: `10.1016/j.energy.2022.125574`.

[30] Hyungmin Park et al. “Drag Reduction in Flow over a Two-Dimensional Bluff Body with a Blunt Trailing Edge Using a New Passive Device”. In: *Journal of Fluid Mechanics* 563 (Sept. 2006), p. 389. ISSN: 0022-1120, 1469-7645. DOI: `10.1017/S0022112006001364`.

A Setups tested only at NTUA

A.1 VGs for flow separation chordwise placement

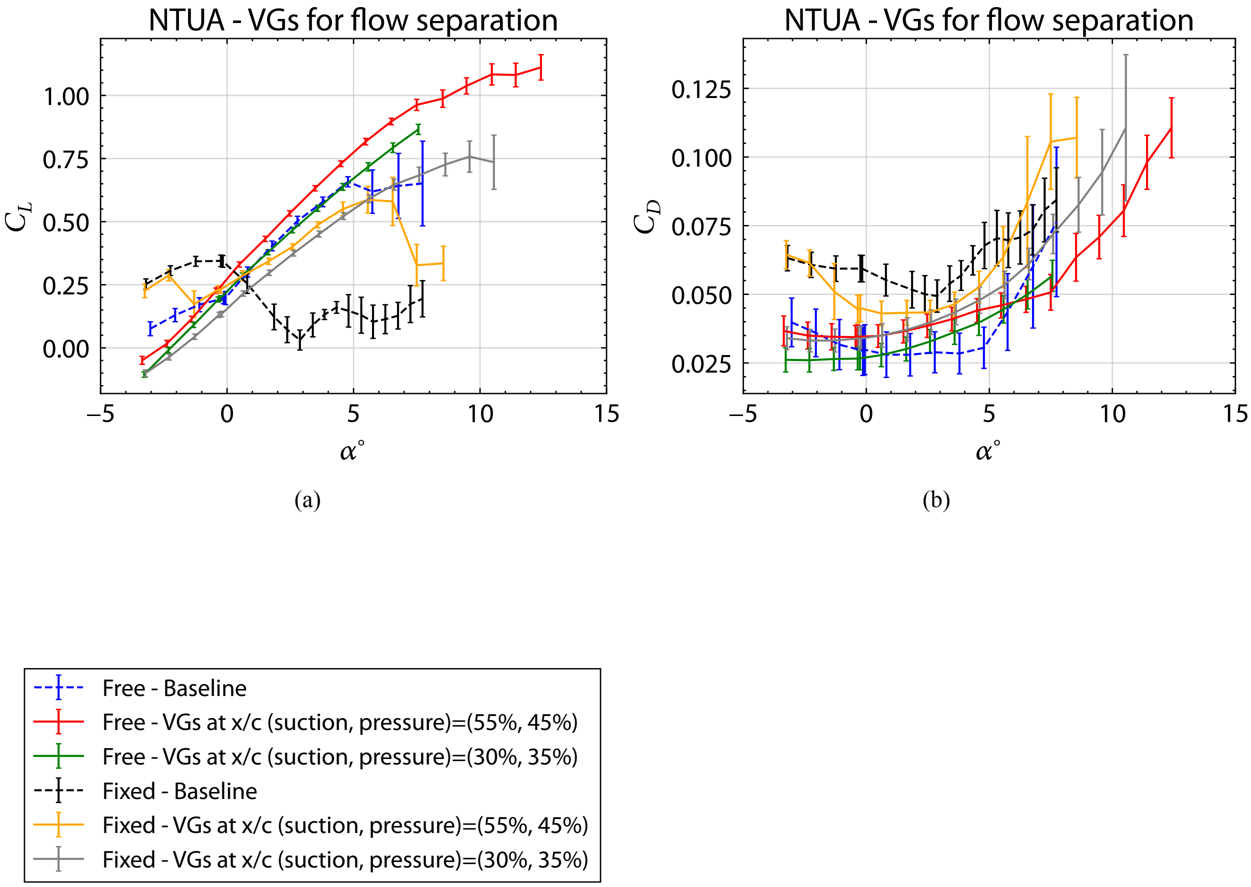

(a)

(b)

(c)

Figure 39: Polars for different chordwise placements of VGs for flow separation control tested at NTUA (a) C_L, (b) C_D, (c) Legend.

A.2 VGs for drag reduction spacing

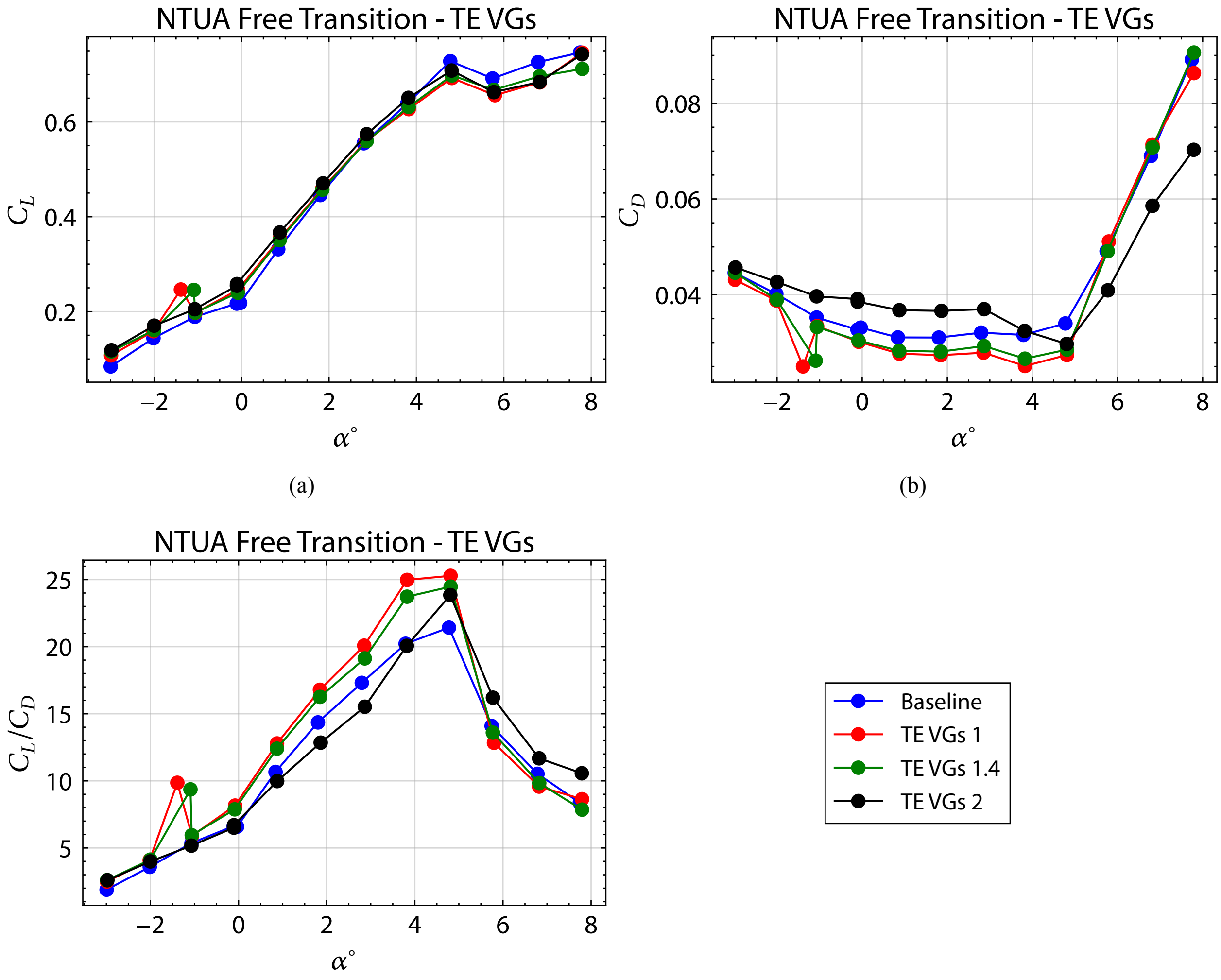

(a)

(b)

(c)

(d)

Figure 40: Polars for different spacings between pairs of VGs used for drag redution. The transition of the BL is free and the cases were evaluated at NTUA (a) C_L, (b) C_D, (c) C_L/C_D.

A.3 TE tabs Spacing

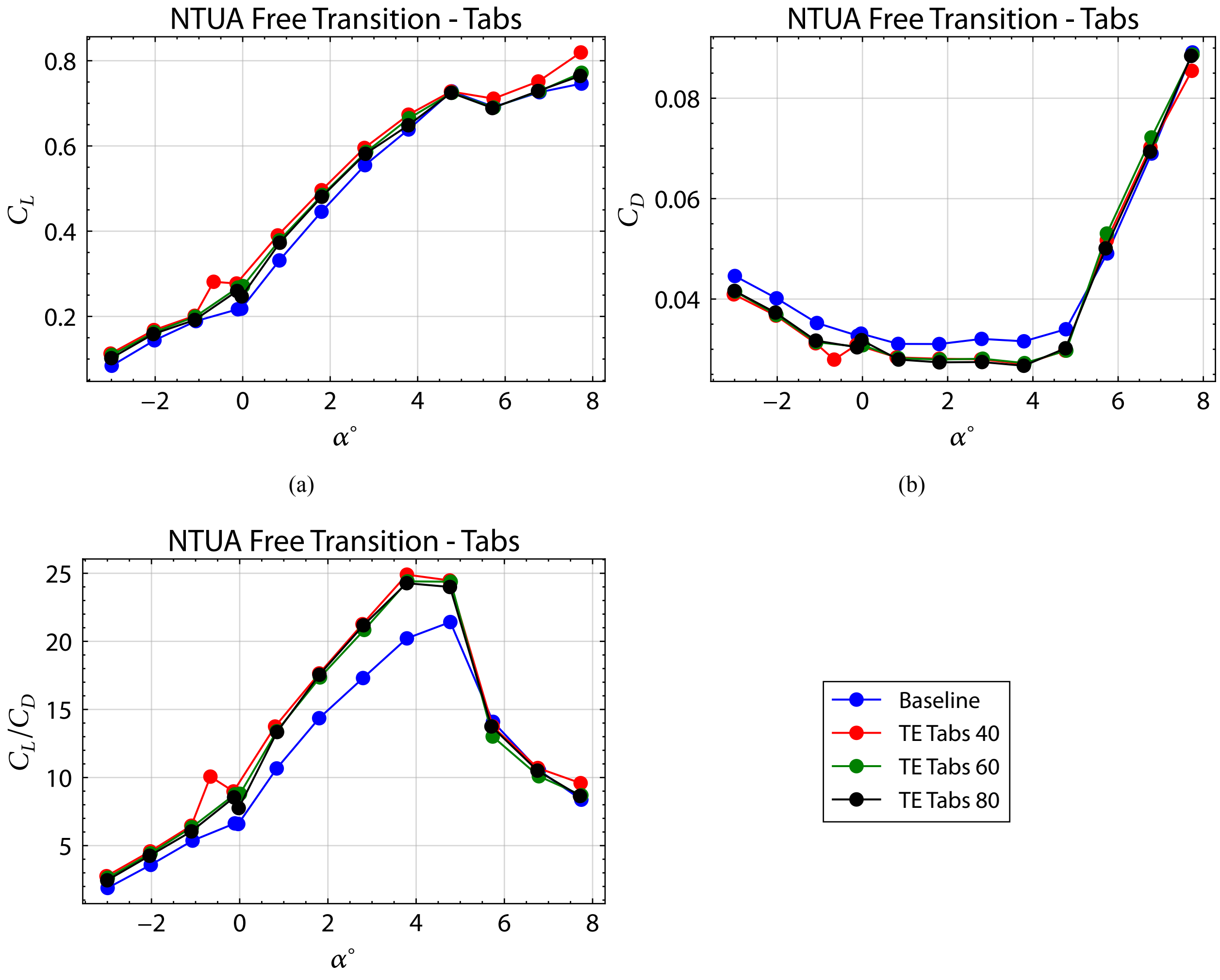

(a) (b)

(c) (d)

Figure 41: Polars for different TE tabs spanwsie spacing for free BL transition evaluated at NTUA (a) C_L, (b) C_D, (c) C_L/C_D.

A.4 GF designs

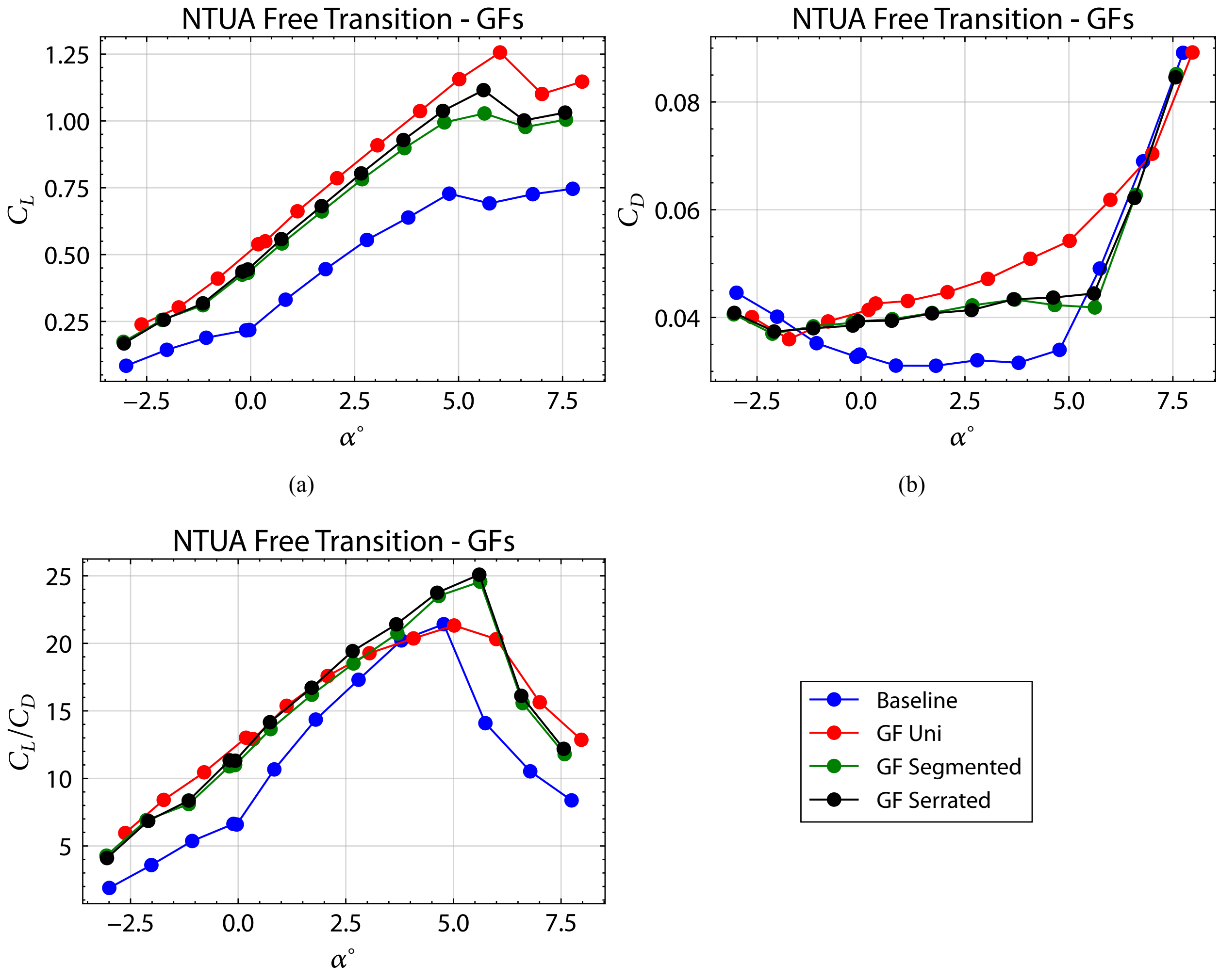

(a) (b)

(c) (d)

Figure 42: Polars for different Gurney flap designs for free BL transition evaluated at NTUA (a) C_L, (b) C_D, (c) C_L/C_D.

Co-funded by
the European Union